# Supporting Information for: XAFS Investigation of Polyamidoxime-Bound Uranyl Contests the Paradigm from Small Molecule Studies

C. W. Abney,[a,b]* R. T. Mayes,[b] M. Piechowicz,[a] Z. Lin,[a] V. S. Bryantsev,[b] G. M. Veith,[b] S. Dai,[b] and W. Lin[a]*

[a.] The University of Chicago, 929 East 57th Street, Chicago, Illinois 60637, United States

[b.] Oak Ridge National Laboratory, P.O. Box 2008, Oak Ridge, Tennessee 37831-6181, United States

abneycw@ornl.gov
wenbinlin@uchicago.edu

## 1. Experimental

### *1.1 General Experimental*

All chemicals were obtained from Fisher Scientific or Sigma Aldrich. Uranyl acetate dihydrate was obtained from Ted Pella, Inc. and used without purification as a standard, as well as to prepare uranyl nitrate according to a literature procedure.[1] All other chemicals and solvents were used without further purification or treatment. Pristine amidoxime-functionalized polymer fibres prepared by RIGP[2] were obtained from ORNL. Amidoxime-functionalized polymer fibres, originally prepared at ORNL, were obtained from PNNL after 1 hr KOH activation and 56 days exposure to filtered seawater from the Sequim Bay.[3, 4] Details pertaining to the KOH activation procedure are provided in section 3.2.3.1.

$^1$H NMR spectra were recorded on a Bruker NMR 500 DRX spectrometer at 500 MHz and referenced to the proton resonance resulting from incomplete deuteration of the $CDCl_3$ (δ 7.26) or DMSO-$d_6$ (δ 2.50). Thermogravimetric analyses (TGA) were performed in air using a Shimadzu TGA-50H equipped with a platinum pan, heated at 2 °C per minute until 300 °C, then at 10 °C per minute until 600°C. Powder X-ray diffraction (PXRD) was performed on a Bruker D8 X-ray diffractometer using Cu radiation and equipped with a sensitive area detector. ICP-MS data were obtained with an Agilent 7700x ICP-MS and analyzed using ICP-MS MassHunter version B01.03. Samples were diluted in a 2% $HNO_3$ matrix and analyzed with a $^{207}$Bi internal standard against a six-point standard curve over the range from 0.1 ppb to 1000 ppb. The correlation coefficient was > 0.9997 for all analyses of interest. Data collection was performed in Spectrum Mode with five replicates per sample and 100 sweeps per replicate. Raman spectra were collected on a Horiba LabRamHR Evolution confocal Raman microscope with a laser wavelength of 633 nm. Total Attenuated Reflectance-FTIR (ATR-IR) spectra of seawater-contacted fibres were collected with a Thermo Nicolet Nexus 670 FT-IR with ATR attachment. ATR-IR spectra of pristine fibres and simulant-contacted fibres were collected with a Perkin Elmer Frontier FTIR with a single-bounce diamond attenuated total reflectance accessory.

X-ray photoelectron spectroscopy (XPS) data were collected using a PHI 3056 spectrometer with an Al anode source operated at 15 kV and an applied power of 350 W. Adventitious carbon was used to

calibrate the binding energy shifts of the sample C1s = 284.8 eV. High resolution data was collected at pass energy of 5.85 eV with 0.05 eV step sizes and a minimum of 60 scans to improve the signal to noise ratio; lower resolution survey scans were collected at pass energy of 93.5 eV with 0.5 eV step sizes and a minimum of 25 scans.

*1.2 Synthesis of Small Molecule Standards*

*1.2.1 Synthesis of Benzamidoxime* Benzamidoxime was prepared following a slightly modified protocol from the literature.[5, 6] In a 25-mL round-bottom flask, 1 g (1 mL, 9.7 mmol) benzonitrile was combined with 0.96 g hydroxylamine (50% in water) (1.5 e.q, 0.89 mL, 14.55 mmol). To this slurry, 10 mL ethanol were added with stirring. The solution was refluxed at 80 °C and monitored by thin-layer chromatography. After 24 hr of reflux, the solution was cooled to room temperature. The solvent was concentrated under vacuum, 10 mL water were added, and the product was extracted three times with $CH_2Cl_2$. The organic phase was dried with $MgSO_4$ and the solvent removed under vacuum to yield the crude product. The pure product was obtained following chromatographic purification in 1:1 EtOAc:$CH_2Cl_2$, yielding 1.14 g (8.4 mmol, 87% yield) of a white crystalline solid. The $^1$H NMR spectra was confirmed against the spectra available in the literature.

*1.2.2 Synthesis of Glutarimidedioxime* Glutarimidedioxime was prepared following a slightly modified protocol from the literature.[7] In a 100-mL glass pressure vessel with threaded Teflon cap, 5 mL EtOH and 6 mL $H_2O$ were combined. 872 mg NaOH (21.8 mmol) were added and stirred until fully dissolved. 1.556 g $NH_2OH$•HCl (21.8 mmol) were gradually added over 15 minutes with stirring, allowing full dissolution before further addition. 500 μL (5.26 mmol) glutaronitrile was added by syringe. The vessel was sealed with the Teflon cap, immersed in oil, and heated at 85 °C with stirring. After 5 days, the vessel was removed from heat and allowed to cool naturally to room temperature. White precipitate was observed as the reaction solution cooled. 170 mg fibrous white solid was collected by filtration (1.19 mmol, 5.5% yield). The $^1$H NMR spectra was confirmed against the spectra available in the literature.

*1.2.3 Preparation of Uranyl Benzamidoxime Crystals* Single crystals of $UO_2$(Benzamidoximate)$_2$(MeOH)$_2$ were obtained following a slightly modified protocol from the literature.[5] In several ½ dram vials, 5 mg $UO_2(NO_3) \cdot 6\ H_2O$ were combined with 4 mg benzamidoxime in 500 µL MeOH to yield dark red solutions. To each solution-containing vial were added 8 – 10 molecular sieves (4Å) which had previously been soaked in triethylamine and had not been subsequently heated or otherwise re-activated. The vials were tightly capped and allowed to sit under ambient light and temperature for 9 days, yielding discrete dark red crystals of the intended complex. The identity of the crystal was confirmed by PXRD, as shown in Figure 3.2. Several crystals were crushed with a needle in the mother liquor, consolidated into a sphere with paratone oil, and fixed to the tip of a Mite-gen crystal holder for analysis. Peak positions and intensities closely match those of the simulated PXRD.

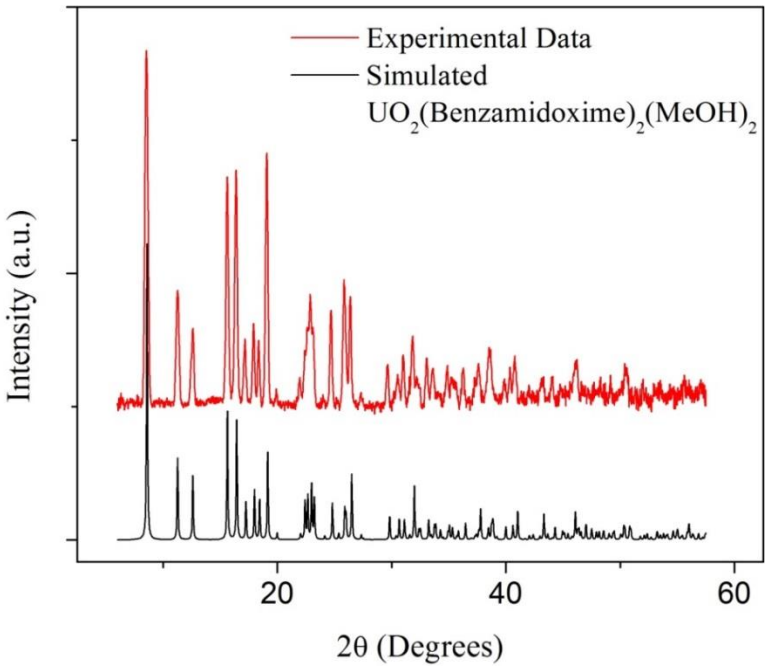


**Figure S1**. PXRD of $UO_2$(Benzamidoximate)$_2$(MeOH)$_2$ compared against the simulated PXRD spectrum.

*1.2.4 Preparation of Uranyl Glutarimidedioxime Crystals* Small single crystals and polycrystalline material of $UO_2$(Glutarimidedioximate)$_2$ were prepared by a slightly modified literature protocol.[7] In several ½ dram vials, 2 mg $UO_2(NO_3)$ • 6 $H_2O$ were combined with 1.144 mg glutarimidedioxime in 920 μL DI water with 80 μL 0.1M aqueous NaOH. The vials were tightly capped and allowed to sit under ambient light and temperature for 7 days, yielding tan polycrystalline powder of the desired complex. The identity of the crystal was confirmed by PXRD, as shown in Figure 3.3. Crystals were collected by centrifugation, suspended in EtOH and drop-cast onto a crystalline Si wafer. Due to formation of polycrystalline material, no grinding was necessary to obtain a uniform thin film. Peak positions and intensities closely match those of the simulated PXRD.

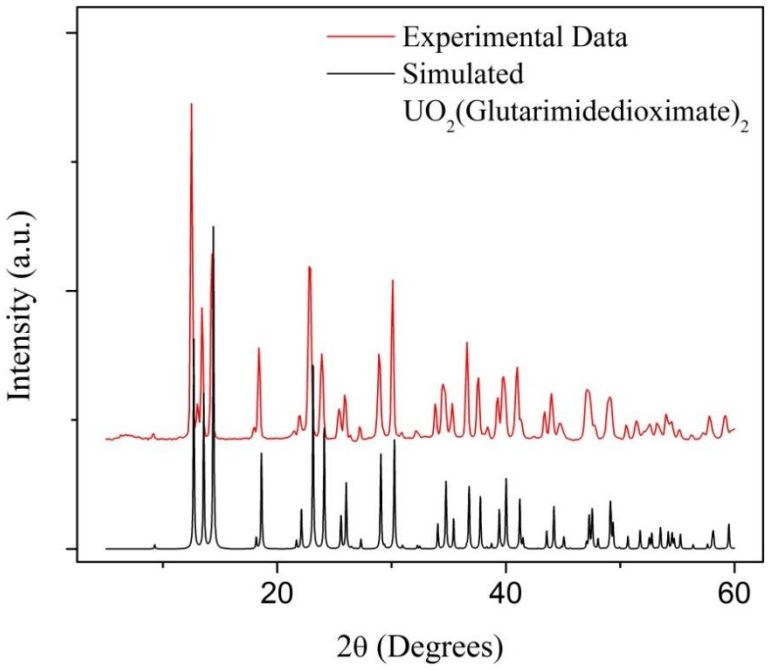


**Figure S2**. PXRD of $UO_2$(Glutarimidedioximate)$_2$ compared against the simulated PXRD spectrum.

*1.3 Preparation of Polymer Fibres*

*1.3.1 KOH Pre-treatment of Amidoxime-Functionalized Polymer Fibres* Treatment of amidoxime-functionalized polymer sorbents with KOH solution prior to deployment is known to dramatically improve uranyl sorption.[8-12] Pre-treatment of the pristine amidoxime-functionalized fibres

were performed by the same protocol used to pre-treat fibres prior to seawater testing at PNNL.[4] 25 mg (dry weight) fibres were soaked in 25 mL of an aqueous 2.5% KOH solution at 80 °C for 1 hr. The fibres were collected by gravity filtration; to preserve the fibre hydrogel, vacuum was not pulled on the fibres at any point. Fibres were washed extensively with DI water until their pH returned to 7-8. Fibres were stored in DI water at pH 7-8 until use.

*1.3.2 Sorption of Uranium by KOH-Treated Fibres in Seawater Simulant* Following KOH treatment, batches of fibres were used to extract uranium from seawater simulant solution, the composition of which is provided in Table 1.[3, 4] To minimize the necessary contact time, uranium is added at a concentration of 8 ppm rather than the environmental concentration of 3.3 ppb. Vanadium is one of the major competing ions for uranium extraction from seawater, and is known to significantly decrease the sorption efficiency for amidoxime-functionalized polymer fibres. To investigate whether the presence of vanadium affects the binding motif of uranium, one batch of seawater simulant was prepared with only uranium, while the other batch also contained 5.3 ppm vanadium from the addition of sodium orthovanadate. No other competing metal ions were added to the seawater simulant solutions.

KOH-treated amidoxime-functionalized polymer fibres (25 mg dry weight, prior to KOH treatment) were suspended at a phase ratio of 25 mg $L^{-1}$ in the two seawater simulant solutions and agitated at 200 RPM on a plate shaker for 24 hrs contact time. Fibres were collected by filtration, washed with DI water, and dried for 24 hrs under vacuum. Uptake of uranium and vanadium was determined by ICP-MS analysis of the stock solutions and supernatant after sorption.

**Table S1** Composition of Seawater Simulant[3, 4]

| **Chemical** | **Mass ($L^{-1}$)** |
|---|---|
| $UO_2(NO_3)_2 \cdot 6\ H_2O$ | 17 mg |
| $Na_3VO_4$ | 19 mg |
| NaCl | 25.6 g |
| $NaHCO_3$ | 194 mg |

*1.3.3 Treatment of Environmental Seawater-Contacted Fibres* Amidoxime-functionalized polymer fibres were contacted with filtered environmental seawater from Sequim Bay in flow-through experiments performed at PNNL, as published previously.[4] In short, fibres were pre-treated with KOH as discussed above, rinsed with DI water, and packed in flow-through columns for exposure to seawater. After 42 days contact time, the samples were rinsed with DI water to remove salts and stored in DI water until sample preparation.

Seawater is known to contain significant quantities of ions capable of competing with uranium for binding sites. Table 2 displays the concentration of metals in the environmental seawater, as well as previously reported amounts adsorbed by polymer fibres of similar formulation.[4] One environmental fibre sample was prepared for XAFS analysis "as received," while a second fibre sample was stripped of all elements other than uranium and vanadium, as reported in the literature.[13] To perform the elution process, 2 g fibres (wet-mass, as received) were washed with DI water and collected by gravity filtration. They were subsequently immersed in 22.5 mL of an aqueous 0.05 M HCl solution containing 1.125 g (5% w/v) L-ascorbic acid and heated overnight at 30 °C. The fibres were collected by gravity filtration and washed with DI water. They were then immersed in 22.5 mL aqueous 0.05 M HCl solution containing 240 mg (1% w/v) thiourea, heated at 30 °C for 2.5 hrs, collected by gravity filtration and washed with DI water. Both batches of polymer fibres, as received and post-elution, were first dried on a Buchner funnel, then dried under vacuum for 24 hrs. Each batch yielded ca. 65 mg dry fibres.

Dry seawater-exposed fibre samples were digested and analyzed by ICP-MS to determine the quantity of uranium, vanadium, and other metals on the fibres. 10.4 mg (dry weight) fibres as received and 11.6 mg fibres post-elution were digested as discussed in the literature.[4] Fibres were immersed in 4 mL of a 3:1 TraceMetal Grade HCl:$HNO_3$ solution and agitated at 300 RPM on a plate shaker for 24 hrs. The fibres which had been eluted with 0.05 M HCl did not dissolve completely and an additional 4 mL acid were added followed by subsequent 24 hrs agitation. Samples were diluted with 18 MΩ DI water, filtered through an 0.2 μm PES syringe filter, and analyzed by ICP-MS as discussed in Section 1.1.

**Table S2** Concentration of Metals in Field Test Seawater and as Adsorbed by Polymer Fibres

| Element | Filtered Seawater (ng/kg) | Metal on Amidoxime Fibre (mg Metal / g Fibre) | | | | |
|---|---|---|---|---|---|---|
| | | Lit. | Simulant (no V)[a.] | Simulant (with V)[a] | Seawater (As Received) | Seawater (Post-Elution) |
| V | 1480 | 5.7 | > 0.1 | 107 ± 5 | 5.8 ± 0.3 | 3.1 ± 0.2 |
| U | 2840 | 2.7 | 165 ± 8 | 62 ± 3 | 3.1 ± 0.2 | 2.9 ± 0.2 |
| Fe | 2200 | 1.9 | --- | --- | 0.8 ± 0.1 | 0.2 ± 0.1 |
| Cu | 540 | 1.3 | --- | --- | 0.7 ± 0.1 | 0.6 ± 0.1 |
| Ni | 560 | 0.7 | --- | --- | 0.4 ± 0.1 | 0.1 ± 0.1 |
| Zn | 2100 | 0.7 | --- | --- | 0.9 ± 0.1 | < 0.1 |
| Sr | --- | 0.3 | --- | --- | 0.1 ± 0.1 | < 0.1 |
| Cr | 180 | 0.2 | --- | --- | < 0.1 | < 0.1 |
| Mn | 1200 | 0.1 | --- | --- | < 0.1 | < 0.1 |
| Pb | 2.5 | 0.1 | --- | --- | < 0.1 | < 0.1 |

[a.] ICP-MS analysis was not performed for metals other than U and V for samples exposed to seawater simulant.
For all ICP-MS measurements, uncertainties were estimated at ±5% of the measured value.

## 2. Low-Energy Spectroscopy

*2.1 Raman Spectroscopy*

Raman spectra were collected for seawater-contacted fibres as well as both batches of simulant-contacted fibres (U only), pristine fibres, and both small molecule standards. Fibres contacted in simulant with both U and V were not analyzable, due to excessive fluorescence from bound V. Data are displayed in **Figure S3**. While features attributable to uranyl can be identified in small molecule standards and simulant-contacted fibres, the concentration of uranium on seawater-contacted fibres is insufficient for meaningful interpretation of the resulting Raman spectra.

*2.2. ATR-FTIR Spectra*

ATR-IR spectra were collected for seawater-contacted fibres as well as both batches of simulant-contacted fibres (U only), and pristine fibres. Data are displayed in **Figure S4**. Features attributable to uranyl cannot be positively identified in even simulant-contacted fibres, indicating the concentration of uranium on seawater-contacted fibres is insufficient for meaningful interpretation of the resulting ATR-IR spectra.

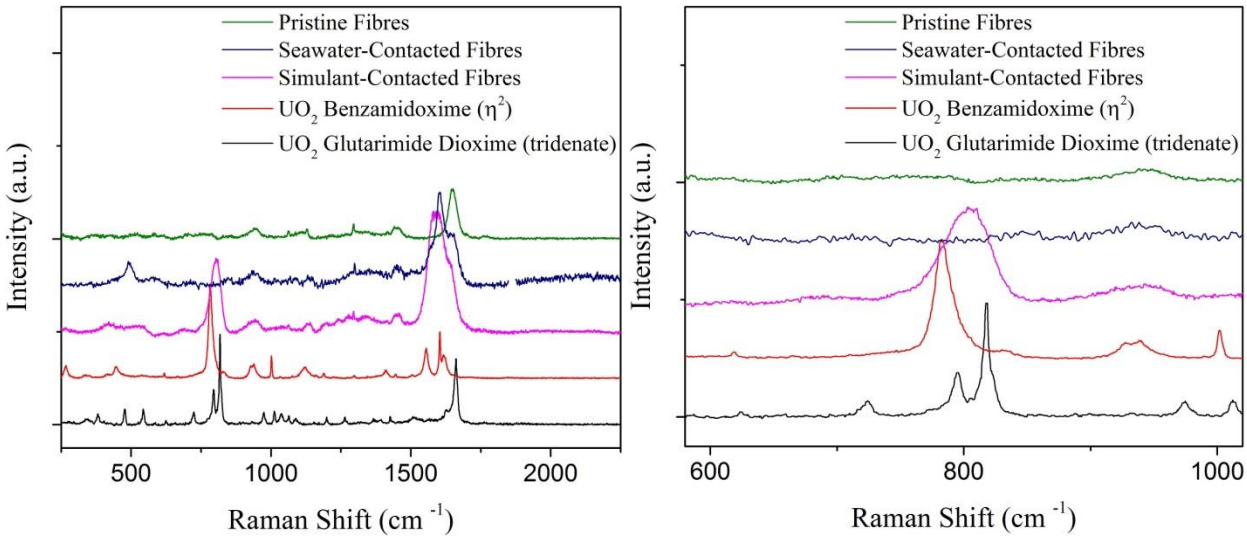


**Figure S3** Raman spectra for fibre samples and small molecule standards. (Left) Raman spectra displayed from 250 – 2500 $cm^{-1}$. (Right) Raman spectra displayed in the region of the strong U-$O_{yl}$ stretching frequency (~800 $cm^{-1}$). Note that no stretching frequency can be observed for the seawater-contacted fibres, revealing the limitations of this form of spectroscopy.

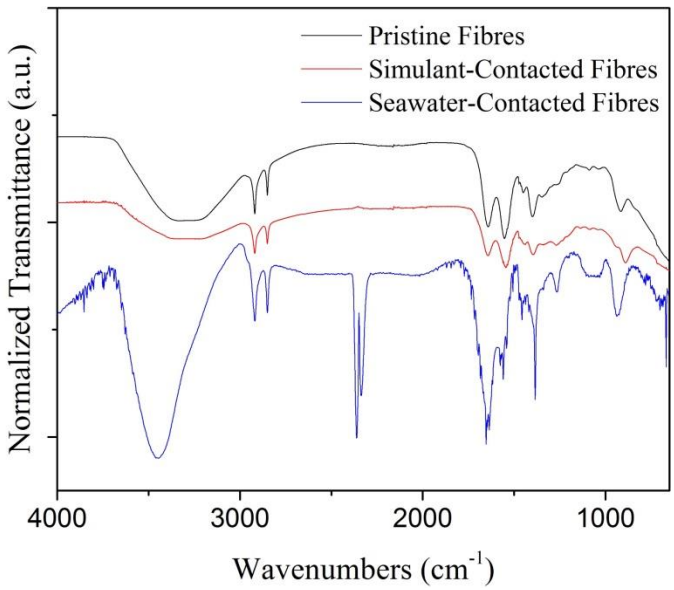


**Figure S4** ATR-IR spectra for pristine fibres, simulant-contacted fibres (U only), and seawater-contacted fibres. No definitive structural information can be obtained from these spectra. The band at approximately 2350 $cm^{-1}$ in the spectra of the seawater-contacted fibers is atmospheric $CO_2$.

## 3. X-ray Absorption Fine Structure Spectroscopy

### *3.1 Preparation of XAFS Standards*

The mass of uranium needed to achieve a 1 – 2.5 absorption length edge step was calculated for each small molecule standard based on the elemental composition and mass absorption coefficient for each element.[14] Small molecule standards were dried under vacuum for 1 hr, ground with an agate mortar and pestle, and blended with D-(+)-Glucose to the appropriate concentration.

For each XAFS sample, approximately 35 mg dry fibres were pulverized using a Retsch CryoMill cryogenic ball mill. Samples were ground in a stainless steel 25 mL grinding jar using 15 mm stainless steel balls. The samples were pre-cooled to cryogenic temperatures for 5 minutes while milling at a rate of 5 hz, then fully pulverized for 5 minutes at 30 hz. An average particle size of 10 μm was obtained by this process. Due to the high concentration of uranium on the simulant-contacted fibres, pulverized fibres were diluted with D-(+)-Glucose to mitigate self-absorption effects.

Approximately 20 – 25 mg of sample (after diluting) was enclosed within a nylon washer of 4.953 mm inner diameter (area of 0.193 $cm^2$), sealed on one side with Kapton film held in place with Kapton tape. The sample was pressed thoroughly by hand to form a firm, uniform pellet, then sealed on the open side with a second piece of Kapton film secured with Kapton tape. The entire sample was placed into a baggie formed of Kapton tape which had been folded in half to prevent any contact with the adhesive. Small pieces of Kapton tape were used to seal the three open edges of the Kapton baggie. This method was approved in advance by the APS Radiation Safety Review Board for achieving the double containment necessary for analysis of radioactive samples.

### *3.2 Data Collection*

The X-ray absorption data were collected at Beamline 10BM-B at the Advanced Photon Source (APS) at Argonne National Laboratory. Spectra were collected at the uranium $L_3$-edge (17166 eV). Data for small molecule crystal standards were collected in transmission mode, while data for uranium-exposed

amidoxime-functionalized polymer fibres were collected by a Hitachi Vortex-ME4 four-element silicon drift fluorescence detector. The X-ray white beam was monochromatized by a Si(111) monochromator and detuned by 50% to reduce the contribution of higher-order harmonics to below the level of noise. The K-edge of an yttrium foil (17038 eV) was used as the reference for energy calibration and measured simultaneously for all samples. The incident beam intensity ($I_0$), transmitted beam intensity ($I_t$), and reference ($I_r$) were all measured by 20 cm ionization chambers with gas compositions of 80% $N_2$ and 20% Ar, 95% Ar and 5% $N_2$, and 100% $N_2$, respectively. All spectra were collected at room temperature.

Samples were centered on the beam and adjusted to find the most homogeneous location in the sample for data collection. The beam was reduced to dimensions of 400 × 3100 μm for all data collection. Data were collected over six regions: -250 to -30 eV (10 eV step size, dwell time of 0.25 seconds), -30 to -5 eV (5 eV step size, dwell time of 0.5 seconds), -5 to 30 eV (1 eV step size), 3 $Å^{-1}$ to 6 $Å^{-1}$ (0.05 $Å^{-1}$ step size, dwell time of 2 seconds), 6 $Å^{-1}$ to 9 $Å^{-1}$ (0.05 $Å^{-1}$ step size, dwell time of 4 seconds), and 9 $Å^{-1}$ to 15 $Å^{-1}$ (0.05 $Å^{-1}$ step size, dwell time of 8 seconds). Three scans were collected at room temperature (~25$^{o}$C) for each sample.

The data were processed and analyzed using the Athena and Artemis programs of the IFEFFIT package based on FEFF 6.[15, 16] Reference foil data were aligned to the first zero-crossing of the second derivative of the normalized μ(E) data, which was subsequently calibrated to the literature $E_0$ for the yttrium K-edge (17038 eV). Spectra were averaged in μ(E) prior to normalization. The background was removed and the data were assigned an Rbkg value of 0.8, slightly less than one-half the value of the half-path length for the nearest scattering element, prior to normalizing to obtain a unit edge step.

All data were initially fit with k-weighting of 1,2, and 3, then finalized with $k^3$-weighting in R-space. Structural parameters that were determined by the fits include the degeneracy of the scattering path ($N_{degen}$), the change in $R_{eff}$ ($\Delta R_i$), the relative mean square displacement of the scattering element ($\sigma^2_i$), the passive electron reduction factor ($S_0^2$), and the energy shift of the photoelectron, ($\Delta E_0$). $S_0^2$ was found to converge to 1.0 ± 0.10 for all fits (standards and polymer fibres) and was thus fixed at that value for all models. Two different $\Delta E$ values were used, one for the tightly-bound axial oxygen and the second

for all other scattering paths.[17, 18] For each fit, the fit range (ΔR), data range (Δk), number of independent points ($N_{idp}$), number of variables ($N_{var}$), degress of freedom (ν), reduced chi-squared value ($\chi_\nu^2$), and R-factor (*R*) are in Table S3. For each fit, the number of independent points was not permitted to exceed 2/3 the number of variables, in keeping with the Nyquist criterion.[18, 19]

**Table S3** Data range and goodness-of-fit parameters for best-fit models

| Sample | ΔR (Å) | Δk (Å$^{-1}$) | $N_{idp}$ | $N_{var}$ | ν | $\chi_\nu^2$ | *R* (%) |
|---|---|---|---|---|---|---|---|
| $UO_2$(Benzamidoxime)$_2$ | 1 – 4.0 | 2.5 – 14.0 | 21 | 12 | 9 | 84.0 | 1.2 |
| $UO_2$(Glutarimidedioxime)$_2$ | 1 – 4.0 | 2.3 – 14.0 | 22 | 14 | 8 | 132 | 2.0 |
| Fibres in Simulant (U only) | 1 – 3.5 | 2.3 – 14.0 | 18 | 11 | 7 | 11.6 | 1.4 |
| Fibres in Simulant (U and V) | 1 – 3.5 | 2.6 – 13.9 | 17 | 11 | 6 | 2.7 | 1.3 |
| Fibres from Seawater (as received) | 1 – 3.5 | 2.0 – 14.0 | 19 | 12 | 6 | 6.0 | 1.8 |
| Fibres from Seawater (post-elution) | 1 – 3.5 | 2.3 – 12.7 | 16 | 10 | 6 | 4.5 | 3.5 |

## 4. XANES Analysis and Linear Combination Fitting

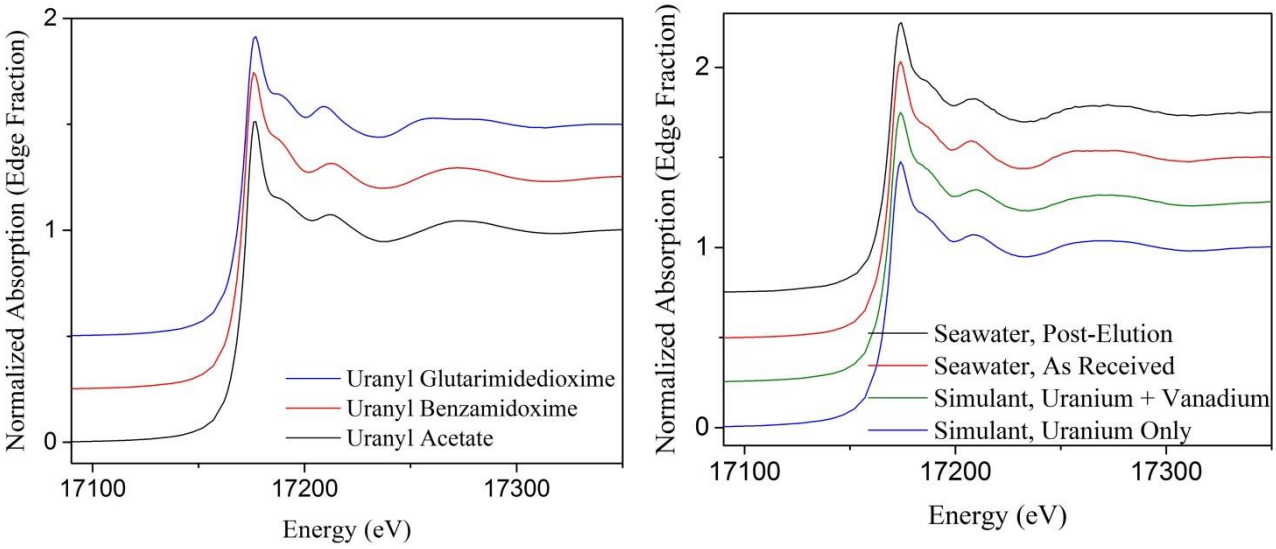


**Figure S5** XANES region of small molecule standards and uranyl acetate dehydrate (left) and uranyl-exposed polymer fibre samples (right) measured at the uranium $L_3$-edge. Normalized absorption spectra are offset by an edge fraction of 0.25 for the sake of clarity.

The absence of any pre-edge feature, a common oxidation state, and similar coordination environment for all samples result in a XANES region with few substantial differences between small molecule standards or polymer-bound uranium samples. It is known the first feature in the XANES region, at approximately 17225 eV, can be attributed to direct scattering off the axial oxygen of uranyl. The second feature, beginning at approximately 17250 eV, is due to the equatorially-coordinated atoms.[20] It is possible to observe a slight difference in the second feature between the uranyl glutarimidedioxime standard, as compared with uranyl benzamidoxime or uranyl acetate. However, these subtle differences are insufficient for deconvoluting the binding environments on the polymer fibres.

XANES is useful in determining the average oxidation state of the absorbing element, as the position of the edge is related to the valence state. There is no precedent to suggest that uranyl is reduced in seawater to influence the binding environment. Previous work reveals the edge position for U(VI) and U(IV) standards differ by more than 4 eV.[18] Our data were aligned to a Y reference foil for which data were collected simultaneously with data collection for our samples of interest. We estimate the uncertainty in the uranium oxidation state in our small molecule standards to be ± 5%, and qualitative comparison between all samples reveal no appreciable difference in edge position. No significant reduction of U(VI) to U(IV) or mineralization as metallic U(0) is observed. This observation is entirely expected and consistent with volumes of literature.

Linear combination fitting was attempted for all non-eluted adsorbent samples using XANES region spectra from small molecule complexes $UO_2$(Benzamidoximate)$_2$(MeOH)$_2$ and $UO_2$(Glutarimide Dioxime)$_2$ as standards. In all instances, the best fit was achieved using only spectral contributions from the $UO_2$(Benzamidoximate)$_2$(MeOH)$_2$ standard. However, in all instances a relatively large residual remained following the linear combination fit, with the most significant occurring for the seawater-contacted fibres. The tightly-bound axial oxygen and similar equatorial coordination environment results in the similarity for fits of fibres exposed to seawater simulant. As mentioned previously, the lack of unique characteristic features hinders much of the utility of XANES analysis, but the relatively large amount of residual in all linear combination fits suggests the fibre-bound uranium atomic environment is

not represented well using just the small molecule standards. These negative results support our assertion that uranyl is bound by a motif that differs from those predicted computationally or from small molecule studies.

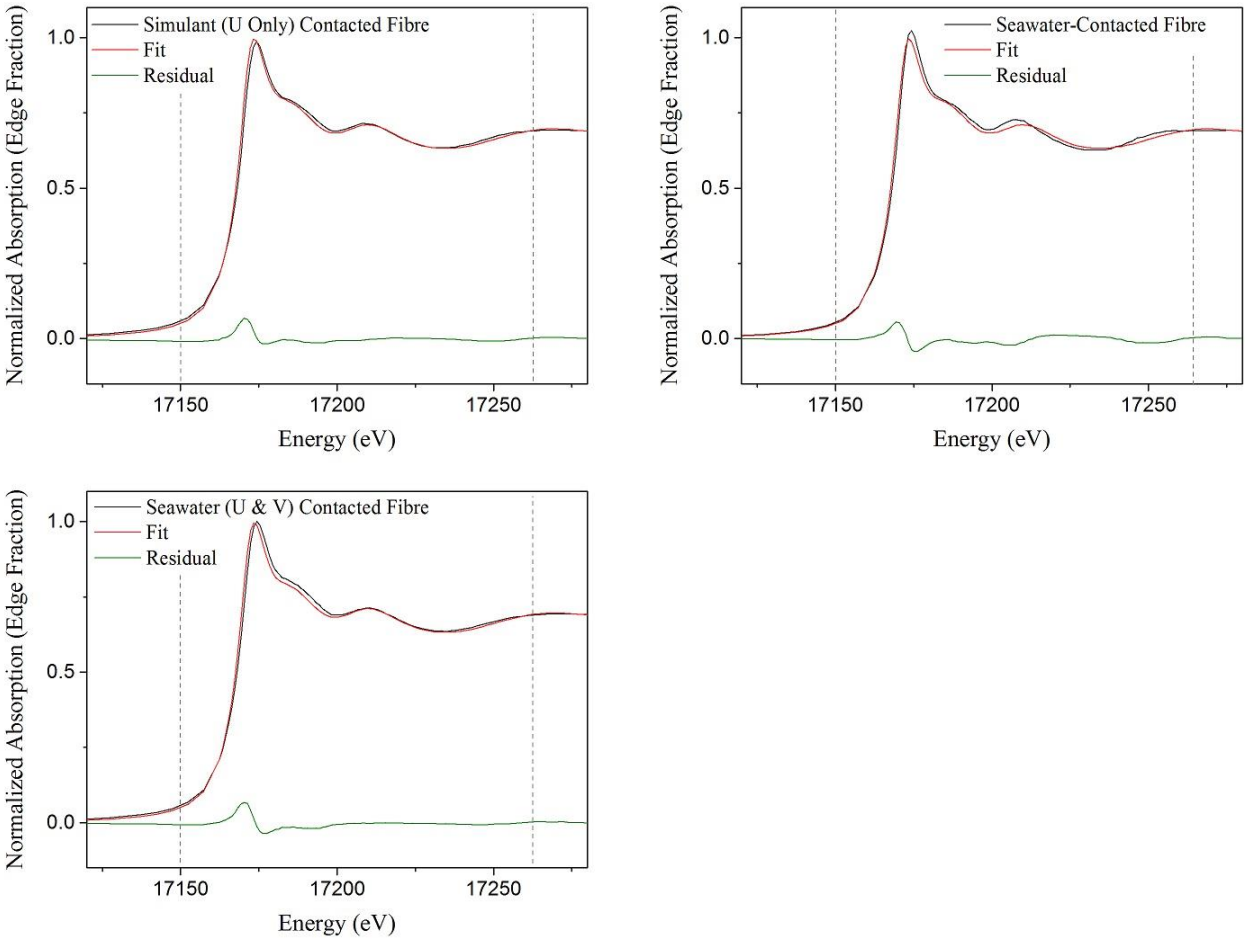


**Figure S6** Linear Combination Fits for (top left) simulant-contacted (U only) polymer fibres, (top right) seawater-contacted polymer fibres, and (bottom left) simulant-contacted (U & V) polymer fibres. XANES data are plotted in black, the best fit is plotted in red, and the residual difference is plotted in green. Despite using both small molecule standards as components in the fit, all best fitted models only used spectral contributions from $UO_2(Benzamidoximate)_2(MeOH)_2$. The large residual suggests this model is a reasonable approximation, but cannot fully resolve all spectral features for the experimental XANES data.

## 5. EXAFS Fitting

### *5.1 Small Molecule Standards.*

*5.1.1 Uranyl Benzamidoxime*. All scattering paths used and parameters determined in the fit of $UO_2$(Benzamidoxime)$_2$ • 2 MeOH are displayed in Table S6. The structure model was based on the obtained single crystal structure of $UO_2$(Benzamidoxime)$_2$• 2 MeOH. (Aside: This single crystal structure was previously reported.[5] The only difference between the single crystal reported herein and the previously reported crystal structure is the temperature at which the structures were obtained. Data was collected at 100K, while data for the previously-reported crystal was collected at 173 K). The best-fit model contains two axial oxygen on uranyl ($O_{yl}$) and direct scattering paths from first shell oxygen (O) and nitrogen (N), and second shell carbon (C). Multiple scattering paths from the axial oxygen contributed to the fits significantly, which can be attributed to strong uranyl binding as well as the linear orientation of $O_{yl}$-U-$O_{yl}$. Other multiple scattering paths included four double scattering paths between the amidoxime oxygen and nitrogen, and two obtuse triangular paths between the amidoxime nitrogen and carbon. The degeneracy of $O_{yl}$ was fixed at two, while the coordination number of O, N, and C were allowed to vary. Change in scattering half-path length ($\Delta R$) and mean squared relative deviation ($\sigma^2$) were free parameters for all direct scattering paths. $\Delta R$ and $\sigma^2$ for $O_{yl}$ was refined simultaneously for both uranyl benzamidoxime and uranyl glutarimidedioxime standards. Errors for multiple scattering pathways were obtained by standard propagation of error from their constituent single scattering pathways.

**Table S4.** Paths, Initial Path Lengths, Initial Degeneracy and Parameters for Fitting Uranyl Benzamidoxime

| Scattering Path | $N_{degen}$ | R(Å) | ΔR (Å) | $\sigma^2$ (Å$^2$) | ΔE |
|---|---|---|---|---|---|
| $U \rightarrow O_{yl}$ | 2 | 1.80 | $\Delta R\text{-}O_{yl}$ | $\sigma^2\text{-}O_{yl}$ | $\Delta E_1$ |
| $U \rightarrow O$ | 4 | 2.35 | ΔR-O | $\sigma^2$-O | $\Delta E_2$ |
| $U \rightarrow N$ | 2 | 2.44 | ΔR-N | $\sigma^2$-N | $\Delta E_2$ |
| $U \rightarrow C$ | 4 | 3.57 | ΔR-C | $\sigma^2$-C | $\Delta E_2$ |
| $U \rightarrow O_{yl(1)} \rightarrow O_{yl(2)}$ | 2 | 3.59 | $2 \times \Delta R\text{-}O_{yl}$ | $2 \times \sigma^2\text{-}O_{yl}$ | $\Delta E_1$ |
| $U \rightarrow O_{yl(1)} \rightarrow U \rightarrow O_{yl(2)}$ | 2 | 3.59 | $2 \times \Delta R\text{-}O_{yl}$ | $2 \times \sigma^2\text{-}O_{yl}$ | $\Delta E_1$ |
| $U \rightarrow O_{yl(1)} \rightarrow U \rightarrow O_{yl(1)}$ | 2 | 3.59 | $2 \times \Delta R\text{-}O_{yl}$ | $2 \times \sigma^2\text{-}O_{yl}$ | $\Delta E_1$ |
| U→N→C | 2 | 3.65 | $0.5 \times \Delta$R-N + $0.5 \times \Delta$R-C | $0.5 \times \sigma^2$-N + $0.5 \times \sigma^2$-C | $\Delta E_2$ |

**Table S5** Best-Fit Values for Uranyl Benzamidoxime Small Molecule Standard

| Scattering Path | $N_{degen}$ | R(Å) | error | | $\sigma^2$ (Å$^2$) | error |
|---|---|---|---|---|---|---|
| $U \rightarrow O_{yl}$ | 2[a] | 1.81 | 0.01 | | 0.002 | < 0.001 |
| U→O | 4 ± 1 | 2.36 | 0.02 | | 0.005 | 0.002 |
| U→N | 2 ± 0.2[b] | 2.51 | 0.03 | | 0.004 | 0.002 |
| U→C | 3 ± 2 | 3.48 | 0.05 | | 0.003 | 0.002 |
| $U \rightarrow O_{yl(1)} \rightarrow O_{yl(2)}$ | 2[a] | 3.62 | 0.01 | | 0.005 | 0.001 |
| $U \rightarrow O_{yl(1)} \rightarrow U \rightarrow O_{yl(2)}$ | 2[a] | 3.62 | 0.01 | | 0.005 | 0.001 |
| $U \rightarrow O_{yl(1)} \rightarrow U \rightarrow O_{yl(1)}$ | 2[a] | 3.62 | 0.01 | | 0.005 | 0.001 |
| U→N→C | 2 ± 0 | 3.64 | 0.03 | | 0.003 | 0.001 |
| $\Delta E_1 = 2 \pm 2$ eV | | | | | | |
| $\Delta E_2 = 1 \pm 2$ eV | | | | | | |

[a] The coordination number for $U \rightarrow O_{yl}$ was held at 2 for the model.

[b] The uncertainty in step height during normalization can be as large as 10%. As $S_0^2$, $N$, and step height are all components of the amplitude, the coordination number cannot be determined to greater accuracy than 10%.[18]

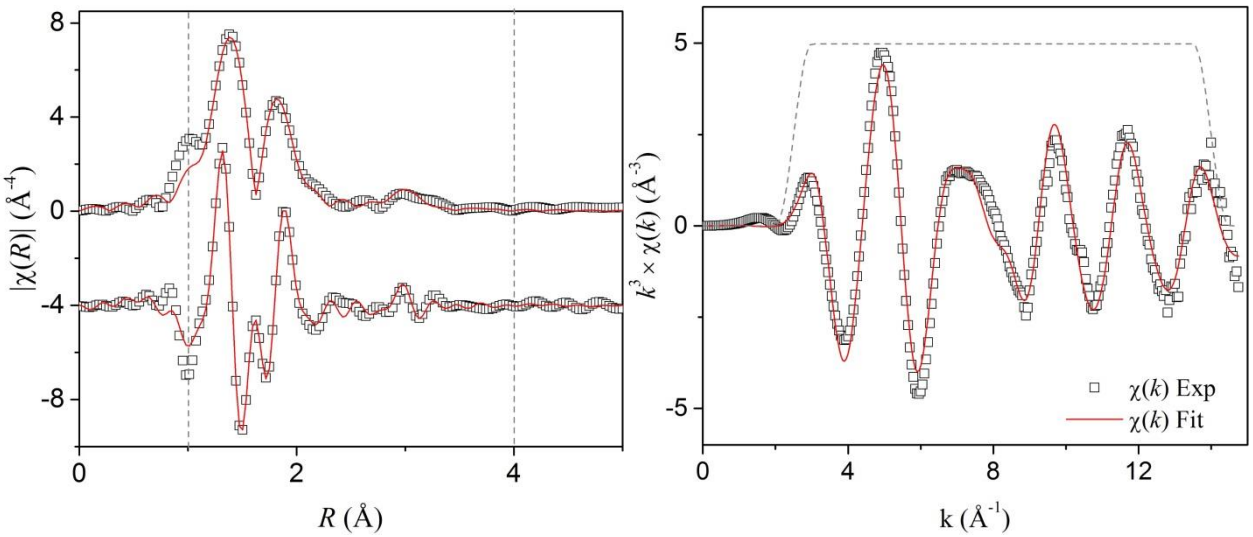


**Figure S7** Data (open symbols) and best-fit model (line) for fit of EXAFS data for uranyl benzamidoxime small molecule standard. The Fourier transform is displayed on the left, with the magnitude (top) and real components. The right column is plotted in k-space. All plots are displayed with $k^3$-weighting. Grey lines display the fitting window.

*5.1.2 Uranyl Glutarimidedioxime*. All scattering paths and parameters determined in the fit of $UO_2$(Glutarimidedioxime)$_2$ are displayed in Table S6. As with uranyl benzamidoxime, strong contributions were required from both direct and multiple scattering off the axial oxygen. Direct scattering paths were from each of the oxime oxygen ($O_{ox1}$, $O_{ox2}$) and nitrogen ($N_{ox}$), the imide nitrogen ($N_{im}$), and the oxime carbon (C). Multiple scattering paths included four obtuse triangular paths between the oxime oxygen and nitrogen, and four obtuse triangular paths between the imide nitrogen and carbon. As with uranyl benzamidoxime, the degeneracy of $O_{yl}$ was fixed at two, while the coordination number of $O_{ox}$ and $N_{im}$, were allowed to vary. The degeneracy of $O_{ox1}$ and $O_{oz2}$ were each equal to 0.5 × the variable $O_{ox}$, and the coordination number of $N_{ox}$ and C were defined as 2 × $N_{im}$. Change in scattering half-path length ($\Delta$R) and mean squared relative deviation ($\sigma^2$) were free parameters for all direct scattering paths, and $\Delta$R and $\sigma^2$ for $O_{yl}$ was refined simultaneously for both uranyl benzamidoxime and uranyl glutarimidedioxime standards. The final evaluated parameters for all scattering paths for both standards

are provided in Table 3.7. Errors for multiple scattering pathways were obtained by standard propagation of error from their constituent single scattering pathways.

**Table S6** Paths, Initial Path Lengths, Initial Degeneracies and Parameters for Fitting Uranyl Glutarimidedioxime

| **Scattering Path** | **$N_{degen}$** | **R(Å)** | **ΔR (Å)** | **$\sigma^2$ (Å$^2$)** | **ΔE** |
|---|---|---|---|---|---|
| $U \rightarrow O_{yl}$ | 2 | 1.79 | $\Delta R\text{-}O_{yl}$ | $\sigma^2\text{-}O_{yl}$ | $\Delta E_1$ |
| $U \rightarrow O_{ox1}$ | 2 | 2.43 | ΔR-O | $\sigma^2$-O | $\Delta E_2$ |
| $U \rightarrow O_{ox2}$ | 2 | 2.53 | ΔR-O | $\sigma^2$-O | $\Delta E_2$ |
| $U \rightarrow N_{im}$ | 2 | 2.56 | $\Delta R\text{-}N_{im}$ | $\sigma^2$-N | $\Delta E_2$ |
| $U \rightarrow N_{ox}$ | 4 | 3.36 | $\Delta R\text{-}N_{ox}$ | $\sigma^2$-N | $\Delta E_2$ |
| U→C | 4 | 3.47 | ΔR-C | $\sigma^2$-C | $\Delta E_2$ |
| $U \rightarrow O_{yl(1)} \rightarrow O_{yl(2)}$ | 2 | 3.57 | $2 \times \Delta R\text{-}O_{yl}$ | $2 \times \sigma^2\text{-}O_{yl}$ | $\Delta E_1$ |
| $U \rightarrow O_{yl(1)} \rightarrow U \rightarrow O_{yl(2)}$ | 2 | 3.57 | $2 \times \Delta R\text{-}O_{yl}$ | $2 \times \sigma^2\text{-}O_{yl}$ | $\Delta E_1$ |
| $U \rightarrow O_{yl(1)} \rightarrow U \rightarrow O_{yl(1)}$ | 2 | 3.57 | $2 \times \Delta R\text{-}O_{yl}$ | $2 \times \sigma^2\text{-}O_{yl}$ | $\Delta E_1$ |
| $U \rightarrow O_{ox} \rightarrow N_{ox}$ | 4 | 3.57 | $0.25 \times \Delta R\text{-}O_{ox1} + 0.25 \times \Delta R\text{-}O_{ox2} + 0.5 \times \Delta R\text{-}N_{ox}$ | $0.5 \times \sigma^2\text{-O} + 0.5 \times \sigma^2\text{-N}$ | $\Delta E_2$ |
| $U \rightarrow N_{ox} \rightarrow C$ | 4 | 3.70 | $0.5 \times \Delta R\text{-}N_{ox} + 0.5 \times \Delta R\text{-C}$ | $0.5 \times \sigma^2\text{-N} + 0.5 \times \sigma^2\text{-C}$ | $\Delta E_2$ |

**Table S7** Best-Fit Values for Uranyl Glutarimidedioxime Small Molecule Standard

| **Scattering Path** | **$N_{degen}$** | **R(Å)** | **error** | | **$\sigma^2$ (Å$^2$)** | **error** |
|---|---|---|---|---|---|---|
| $U \rightarrow O_{yl}$ | 2[a] | 1.80 | 0.01 | | 0.002 | < 0.001 |
| $U \rightarrow O_{ox1}$ | 1.5 ± 1 | 2.42 | 0.02 | | 0.005 | 0.003 |
| $U \rightarrow O_{ox2}$ | 1.5 ± 1 | 2.54 | 0.02 | | 0.005 | 0.003 |
| $U \rightarrow N_{im}$ | 1.5 ± 1 | 2.56 | 0.02 | | 0.003 | 0.001 |
| $U \rightarrow N_{ox}$ | 3 ± 2 | 3.36 | 0.03 | | 0.003 | 0.001 |
| U→C | 3 ± 2 | 3.47 | 0.01 | | 0.004 | 0.002 |
| $U \rightarrow O_{yl(1)} \rightarrow O_{yl(2)}$ | 2[a] | 3.60 | 0.01 | | 0.006 | 0.001 |
| $U \rightarrow O_{yl(1)} \rightarrow U \rightarrow O_{yl(2)}$ | 2[a] | 3.60 | 0.01 | | 0.006 | 0.001 |
| $U \rightarrow O_{yl(1)} \rightarrow U \rightarrow O_{yl(1)}$ | 2[a] | 3.60 | 0.01 | | 0.006 | 0.001 |
| $U \rightarrow O_{ox} \rightarrow N_{ox}$ | 3 ± 2 | 3.59 | 0.02 | | 0.004 | 0.002 |
| $U \rightarrow N_{ox} \rightarrow C$ | 3 ± 2 | 3.71 | 0.02 | | 0.003 | 0.002 |
| $\Delta E_1 = 1 \pm 2$ eV | | | | | | |
| $\Delta E_2 = 2 \pm 2$ eV | | | | | | |

[a] The coordination number for $U \rightarrow O_{yl}$ was held at 2 for the model.

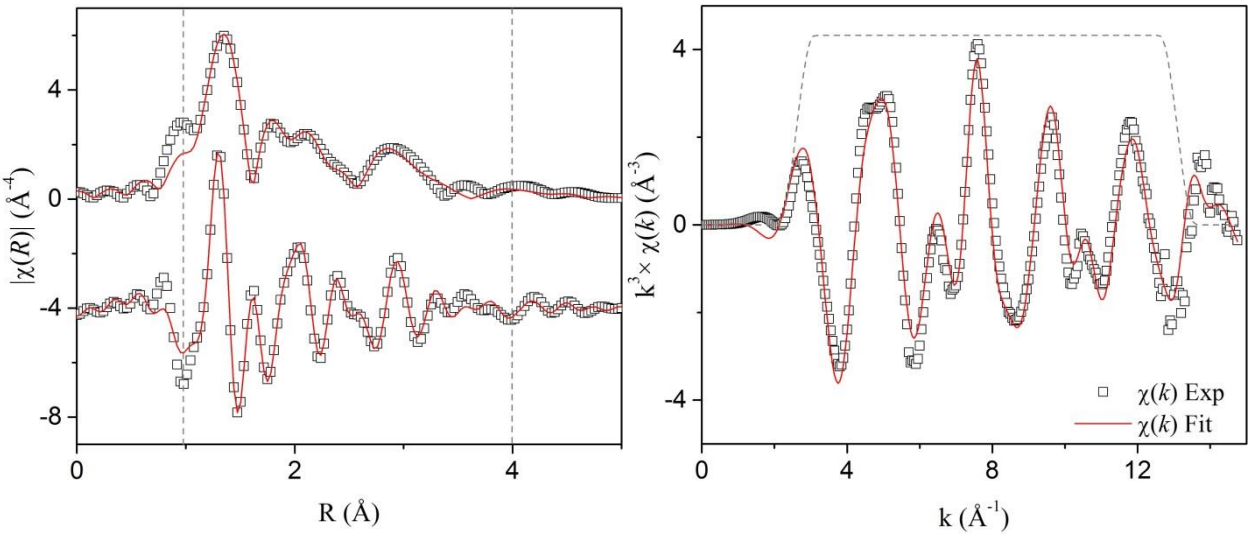


**Figure S8** Data (open symbols) and best-fit model (line) for fit of EXAFS data for uranyl glutarimidedioxime small molecule standard. The Fourier transform is displayed on the left, with the magnitude (top) and real components. The right column is plotted in k-space. All plots are displayed with $k^3$-weighting. Grey lines display the fitting window.

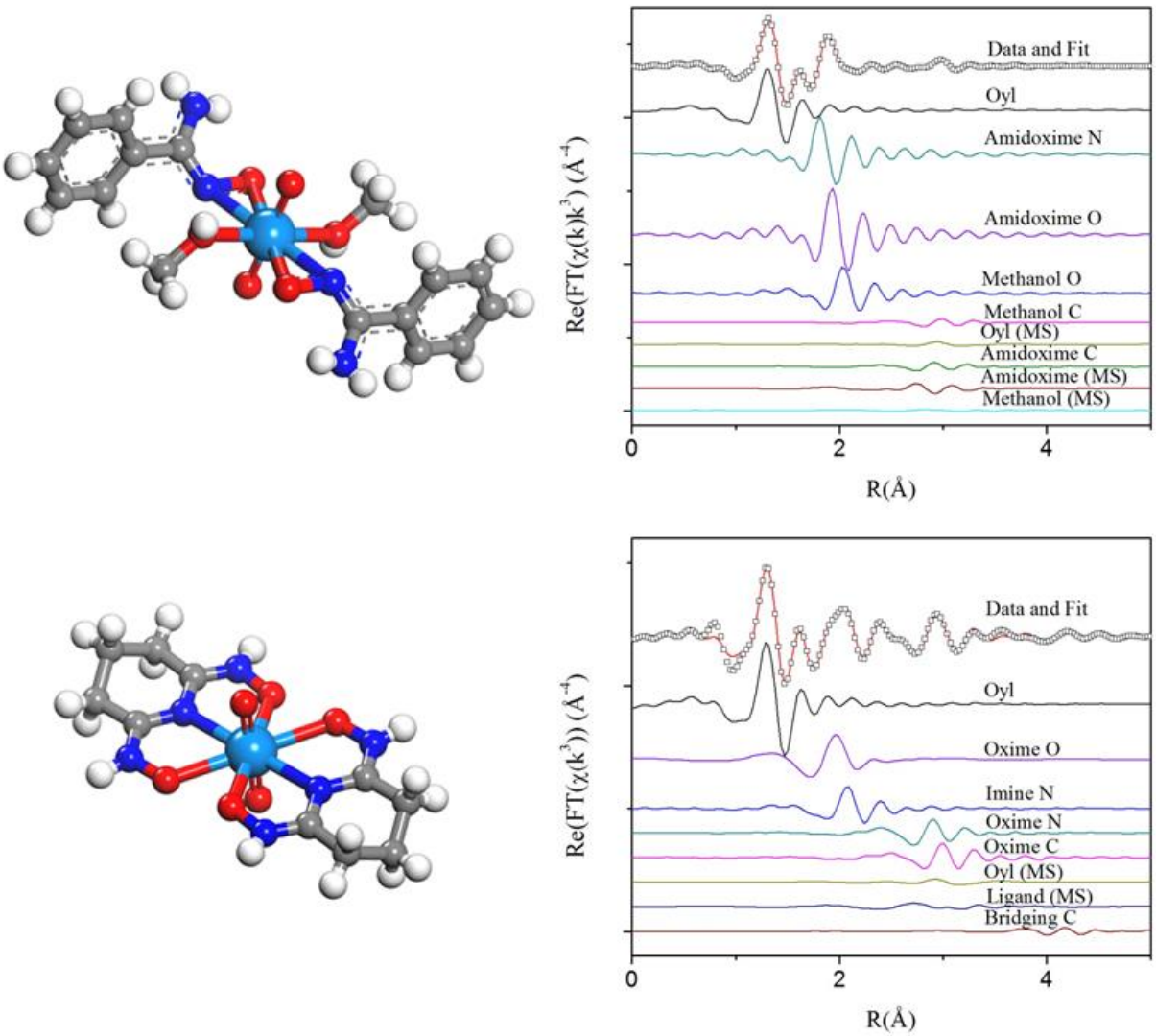


**Figure S9.** The real part of the Fourier transform of the uranium $L_3$-edge EXAFS spectrum (open symbols) and fit (red line) for small molecule standards uranyl benzamidoxime (top) and uranyl glutarimidedioxime (bottom). Components of the fit are displayed below, with the corresponding crystal structure to the left. The crystal structure for uranyl glutarimidedioxime was obtained from the literature.[7] Multiple scattering paths are summed and displayed as one path, denoted by a label containing (MS).

*5.2 Polymer Fibres*

Fits of polymer fibre data were attempted in a bottom-up fashion using models representative of each of the four proposed binding configurations. While more distant scattering paths were progressively included, refined values for previously established scattering paths were used as initial guesses, but allowed to vary freely to avoid introduction of systematic error. For all models, equatorial light scatterers converged to approximately 5-6 atoms, consistent with previous XAFS and crystallographic studies. Scattering paths were added one at a time for different elements at different distances and evaluated in the real-space component of the Fourier transform. Paths which required indefensible changes in scatterer half-path length or mean squared relative deviation were discarded. Paths representative of carbonate were investigated for all polymer fibres, while paths representative of phosphates, $\mu_2$-oxo bridging Cu, Fe, Zn, Ni, and V, and Na, Ca, and Mg cations were considered for all seawater-contacted fibres. Iterative refinement of the fits resulted in the finalized models discussed below.

*5.2.1 Simulant-Contacted Fibres (Uranium Only).* The model used to fit the fibre data was composed of several shells of light scattering elements. The first shell was composed exclusively of the tightly-bound uranyl axial oxygen ($O_{yl}$) with degeneracy fixed at 2. The second shell was composed of light scatterers at two different distances with equal, but variable degeneracy ($O_1$, $N_1$). The third shell was composed of light scatterers at different distances with equal, but variable degeneracy ($N_2$, C). $\Delta R$ and $\sigma^2$ were free parameters for all direct scattering paths. Degeneracy was a free parameter for all direct scattering paths except $O_{yl}$. This model structure is most consistent with a coordination environment consisting of 2-3 chelating ligands per uranyl. Data were not fit beyond 3.5 Å in R-space due to the large noise in the data.

Of particular note, extensive efforts were made to fit this data using a model representative of $\eta^2$-chelating ligands. A reasonable fit can be obtained with this model, affording an R-factor of 1.8 and a $\chi_v^2$ of 16.5 over the same fitting range. In addition to being a statistically less rigorous fit than that of the chelate model, the magnitude of the fit was consistently lower than the experimental data at higher values of R.

**Table S8** Paths, Initial Path Lengths, Degeneracies, and Parameters for Fitting Polymer Fibres Contacted with Seawater Simulant (Uranium Only)

| Scattering Path | $N_{degen}$ | R(Å) | ΔR (Å) | $\sigma^2$ (Å$^2$) | $\Delta E_1$ |
|---|---|---|---|---|---|
| $U \rightarrow O_{yl}$ | 2 | 1.79 | $\Delta R\text{-}O_{yl}$ | $\sigma^2\text{-}O_{yl}$ | $\Delta E_1$ |
| $U \rightarrow O_1$ | CN_1 | 2.30 | ΔR-O | $\sigma^2$-O | $\Delta E_2$ |
| $U \rightarrow N_1$ | CN_1 | 2.45 | ΔR-O | $\sigma^2$-O | $\Delta E_2$ |
| $U \rightarrow N_2$ | CN_2 | 3.31 | ΔR-N | $\sigma^2$-N | $\Delta E_2$ |
| U→C | CN_2 | 3.47 | ΔR-C | $\sigma^2$-C | $\Delta E_2$ |
| $U \rightarrow O_1 \rightarrow N_2$ | CN_1 | 3.53 | $0.5 \times \Delta R\text{-}O_1 + 0.5 \times \Delta R\text{-}N_2$ | $0.5 \times \sigma^2\text{-O} + 0.5 \times \sigma^2\text{-N}$ | $\Delta E_2$ |
| $U \rightarrow O_{yl(1)} \rightarrow O_{yl(2)}$ | 2 | 3.57 | $2 \times \Delta R\text{-}O_{yl}$ | $2 \times \sigma^2\text{-}O_{yl}$ | $\Delta E_1$ |
| $U \rightarrow O_{yl(1)} \rightarrow U \rightarrow O_{yl(2)}$ | 2 | 3.57 | $2 \times \Delta R\text{-}O_{yl}$ | $2 \times \sigma^2\text{-}O_{yl}$ | $\Delta E_1$ |
| $U \rightarrow O_{yl(1)} \rightarrow U \rightarrow O_{yl(1)}$ | 2 | 3.57 | $2 \times \Delta R\text{-}O_{yl}$ | $2 \times \sigma^2\text{-}O_{yl}$ | $\Delta E_1$ |
| $U \rightarrow O_{yl} \rightarrow O_1$ | 2×CN_1 | 3.70 | $0.5 \times \Delta R\text{-}O_{yl} + 0.5 \times \Delta R\text{-}O_1$ | $0.5 \times \sigma^2\text{-}O_{yl} + 0.5\times \sigma^2\text{-O}$ | $\Delta E_1$ |

**Table S9** Best Fit Values for Polymer Fibres Contacted with Seawater Simulant (Uranium Only)

| Scattering Path | $N_{degen}$ | R(Å) | error | | $\sigma^2$ (Å$^2$) | error |
|---|---|---|---|---|---|---|
| $U \rightarrow O_{yl}$ | 2[a] | 1.80 | 0.01 | | 0.002 | < 0.001 |
| $U \rightarrow O_1$ | 2.8 ± 0.6 | 2.35 | 0.02 | | 0.005 | 0.003 |
| $U \rightarrow N_1$ | 2.8 ± 0.6 | 2.49 | 0.02 | | 0.005 | 0.003 |
| $U \rightarrow N_2$ | 2.8 ± 1.2 | 3.37 | 0.05 | | 0.003 | 0.001 |
| U→C | 2.8 ± 1.2 | 3.48 | 0.03 | | 0.004 | 0.002 |
| $U \rightarrow O_1 \rightarrow N_2$ | 2.8 ± 0.6 | 3.59 | 0.03 | | 0.004 | 0.002 |
| $U \rightarrow O_{yl(1)} \rightarrow O_{yl(2)}$ | 2[a] | 3.60 | 0.01 | | 0.004 | 0.001 |
| $U \rightarrow O_{yl(1)} \rightarrow U \rightarrow O_{yl(2)}$ | 2[a] | 3.60 | 0.01 | | 0.004 | 0.001 |
| $U \rightarrow O_{yl(1)} \rightarrow U \rightarrow O_{yl(1)}$ | 2[a] | 3.60 | 0.01 | | 0.004 | 0.001 |
| $U \rightarrow O_{yl} \rightarrow O_1$ | 5.6 ± 0.4 | 3.59 | 0.01 | | 0.003 | 0.002 |
| $\Delta E_1 = 0 \pm 1$ eV | | | | | | |
| $\Delta E_2 = 2 \pm 2$ eV | | | | | | |

[a] The coordination number for $U \rightarrow O_{yl}$ was held at 2 for the model.

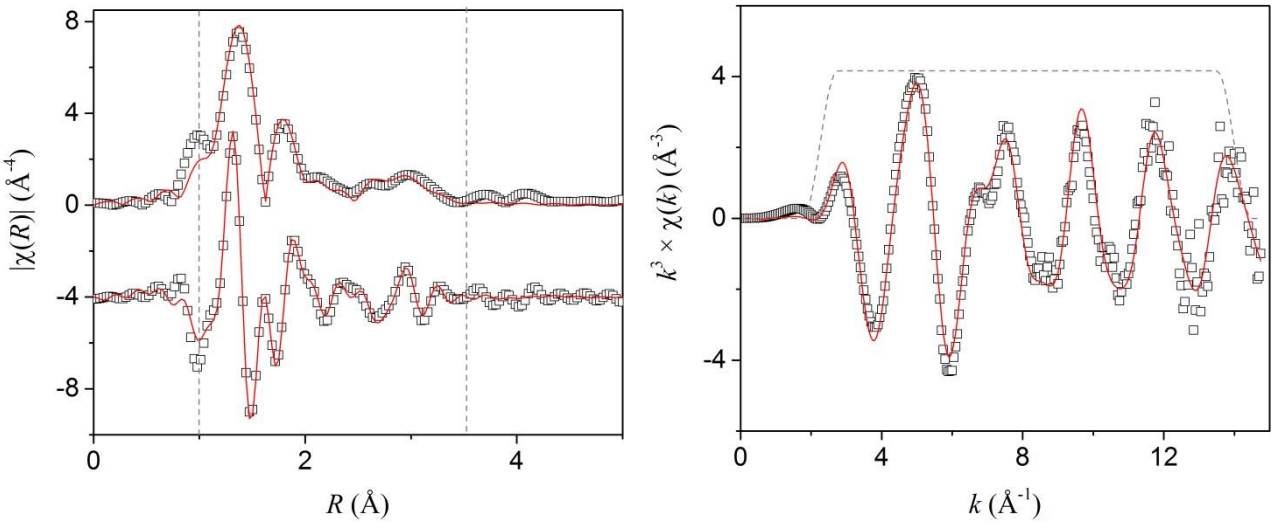


**Figure S10** Data (open symbols) and best-fit chelation model (line) for fit of EXAFS data for polymer fibres contacted with seawater simulant containing uranium (only). The Fourier transform is displayed on the left, with the magnitude (top) and real components. The right column is plotted in k-space. All plots are displayed with $k^3$-weighting. Grey lines display the fitting window.

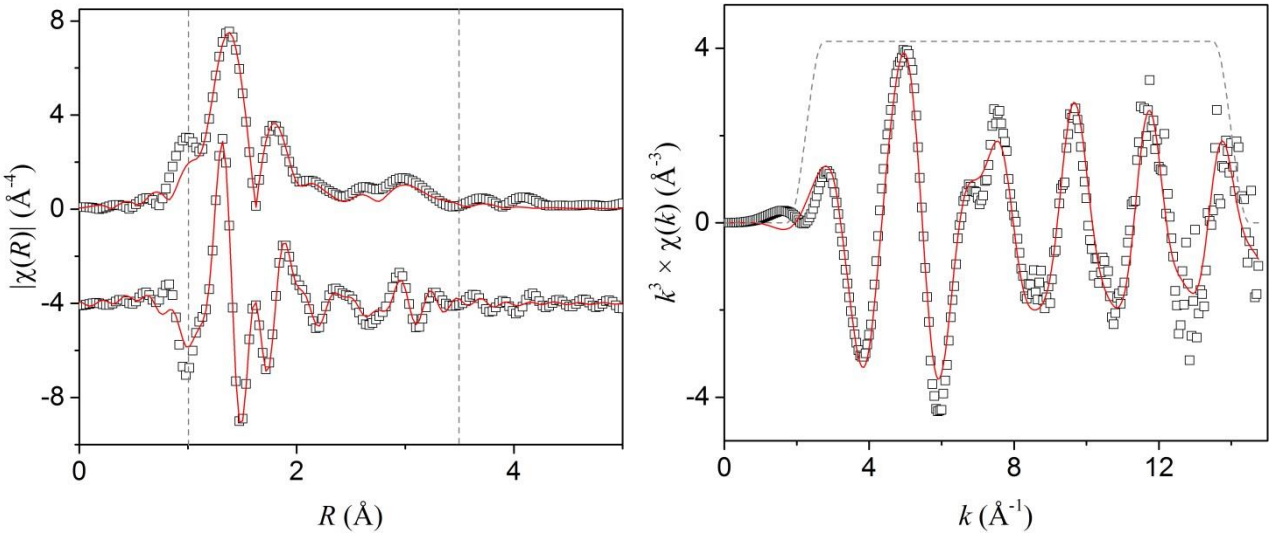


**Figure S11** Data (open symbols) and fit for $\eta^2$-model (line) for fit of EXAFS data for polymer fibres contacted with seawater simulant containing uranium (only). The Fourier transform is displayed on the left, with the magnitude (top) and real components. The right column is plotted in k-space. An R-factor

of 1.8 and a $\chi_v^2$ of 16.5 were obtained for these fits, both of which are higher than metrics obtained for the fit using the chelator model. Also note the systemically lower intensity of the fit at approximately 2.5 - 3Å. At this distance for the $\eta^2$-model, only the oxime carbon and multiple scattering paths are capable of contributing intensity. In contrast, there are approximately 2× the number of atoms at the same distance in the chelating model. All plots are displayed with $k^3$-weighting. Grey lines display the fitting window.

*5.2.2 Simulant-Contacted Fibres (Uranium and Vanadium).* The model used to fit the fibre data was identical to that of simulant-contacted fibres (uranium only). The first shell was composed exclusively of the tightly-bound uranyl axial oxygen ($O_{yl}$) with degeneracy fixed at 2. The second shell was composed of light scatterers at two different distances with equal, but variable degeneracy ($O_1$, $N_1$). The third shell was composed of light scatterers at different distances with equal, but variable degeneracy ($N_2$, C). $\Delta R$ and $\sigma^2$ were free parameters for all direct scattering paths. Degeneracy was a free parameter for all direct scattering paths except $O_{yl}$. This model structure is most consistent with a coordination environment consisting of 2-3 chelating ligands per uranyl. Data were not fit beyond 3.5 Å in R-space due to the large noise in the data.

**Table S10** Paths, Initial Path Lengths, Degeneracies, and Parameters for Fitting Polymer Fibres Contacted with Seawater Simulant (Uranium and Vanadium)

| **Scattering Path** | **$N_{degen}$** | **R(Å)** | **$\Delta$R (Å)** | **$\sigma^2$ (Å$^2$)** | **$\Delta E_1$** |
|---|---|---|---|---|---|
| $U \rightarrow O_{yl}$ | 2 | 1.79 | $\Delta R\text{-}O_{yl}$ | $\sigma^2\text{-}O_{yl}$ | $\Delta E_1$ |
| $U \rightarrow O_1$ | CN_1 | 2.30 | $\Delta R\text{-}O$ | $\sigma^2\text{-}O$ | $\Delta E_2$ |
| $U \rightarrow N_1$ | CN_1 | 2.45 | $\Delta R\text{-}O$ | $\sigma^2\text{-}O$ | $\Delta E_2$ |
| $U \rightarrow N_2$ | CN_2 | 3.31 | $\Delta R\text{-}N$ | $\sigma^2\text{-}N$ | $\Delta E_2$ |
| $U \rightarrow C$ | CN_2 | 3.47 | $\Delta R\text{-}C$ | $\sigma^2\text{-}C$ | $\Delta E_2$ |
| $U \rightarrow O_1 \rightarrow N_2$ | CN_2 | 3.53 | $0.5 \times \Delta R\text{-}O_1 + 0.5 \times \Delta R\text{-}N_2$ | $0.5 \times \sigma^2\text{-}O + 0.5 \times \sigma^2\text{-}N$ | $\Delta E_2$ |
| $U \rightarrow O_{yl(1)} \rightarrow O_{yl(2)}$ | 2 | 3.57 | $2 \times \Delta R\text{-}O_{yl}$ | $2 \times \sigma^2\text{-}O_{yl}$ | $\Delta E_1$ |
| $U \rightarrow O_{yl(1)} \rightarrow U \rightarrow O_{yl(2)}$ | 2 | 3.57 | $2 \times \Delta R\text{-}O_{yl}$ | $2 \times \sigma^2\text{-}O_{yl}$ | $\Delta E_1$ |
| $U \rightarrow O_{yl(1)} \rightarrow U \rightarrow O_{yl(1)}$ | 2 | 3.57 | $2 \times \Delta R\text{-}O_{yl}$ | $2 \times \sigma^2\text{-}O_{yl}$ | $\Delta E_1$ |
| $U \rightarrow O_{yl} \rightarrow O_1$ | 2×CN_1 | 3.70 | $0.5 \times \Delta R\text{-}O_{yl} + 0.5 \times \Delta R\text{-}O_1$ | $0.5 \times \sigma^2\text{-}O_{yl} + 0.5\times \sigma^2\text{-}O$ | $\Delta E_1$ |

**Table S11** Best Fit Values for Polymer Fibres Contacted with Seawater Simulant (Uranium and Vanadium)

| Scattering Path | $N_{degen}$ | R(Å) | error | | $\sigma^2$ (Å$^2$) | error |
|---|---|---|---|---|---|---|
| $U \rightarrow O_{yl}$ | 2[a] | 1.80 | 0.01 | | 0.002 | < 0.001 |
| $U \rightarrow O_1$ | 3.1 ± 0.7 | 2.35 | 0.02 | | 0.006 | 0.002 |
| $U \rightarrow N_1$ | 3.1 ± 0.7 | 2.49 | 0.02 | | 0.006 | 0.002 |
| $U \rightarrow N_2$ | 3.4 ± 1.1 | 3.37 | 0.04 | | 0.006 | 0.002 |
| $U \rightarrow C$ | 3.4 ± 1.1 | 3.48 | 0.02 | | 0.002 | 0.001 |
| $U \rightarrow O_1 \rightarrow N_2$ | 3.1 ± 0.7 | 3.59 | 0.02 | | 0.004 | 0.002 |
| $U \rightarrow O_{yl(1)} \rightarrow O_{yl(2)}$ | 2[a] | 3.60 | 0.01 | | 0.004 | 0.001 |
| $U \rightarrow O_{yl(1)} \rightarrow U \rightarrow O_{yl(2)}$ | 2[a] | 3.60 | 0.01 | | 0.004 | 0.001 |
| $U \rightarrow O_{yl(1)} \rightarrow U \rightarrow O_{yl(1)}$ | 2[a] | 3.60 | 0.01 | | 0.004 | 0.001 |
| $U \rightarrow O_{yl} \rightarrow O_1$ | 6.2 ± 0.5 | 3.59 | 0.01 | | 0.003 | 0.001 |
| $\Delta E_1$ = -2 ± 1 eV | | | | | | |
| $\Delta E_2$ = -1 ± 3 eV | | | | | | |

[a] The coordination number for $U \rightarrow O_{yl}$ was held at 2 for the model.

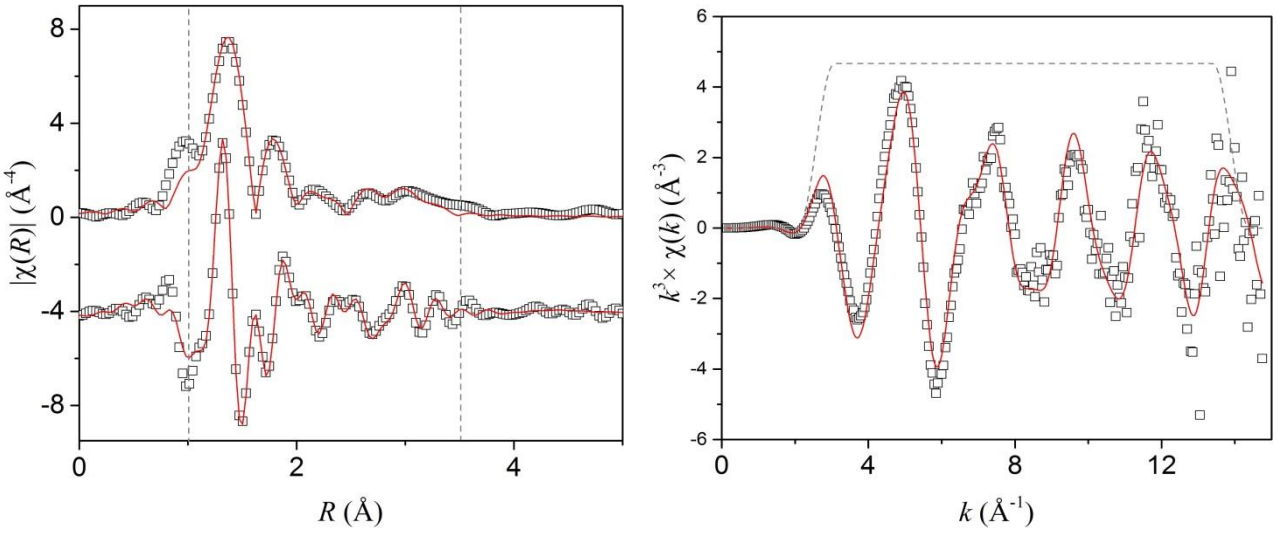


**Figure S12** Data (open symbols) and best-fit chelation model (line) for fit of EXAFS data for polymer fibres contacted with seawater simulant containing uranium and vanadium. The Fourier transform is displayed on the left, with the magnitude (top) and real components. The right column is plotted in k-space. All plots are displayed with $k^3$-weighting. Grey lines display the fitting window.

*5.2.3 Seawater-Contacted Fibres (As Received).* The model used to fit the fibre data was composed of several shells of light scattering elements and one transition metal scatterer. The first shell was composed exclusively of the tightly-bound uranyl axial oxygen ($O_{yl}$) with degeneracy fixed at 2. The second shell was composed of light scatterers at two different distances with equal, but variable degeneracy ($O_1$, $N_1$). The third shell was composed of light scatterers at different distances with equal, but variable degeneracy ($N_2$, C) and a transition metal, Ni. $\Delta R$ and $\sigma^2$ were free parameters for all direct scattering paths, and degeneracy was a free parameter for all direct scattering paths except $O_{yl}$. To comply with the Nyquist criterion, the degeneracy and $\sigma^2$ for $O_1$ and $N_1$ were defined as equivalent, and the degeneracy, $\Delta R$, and $\sigma^2$ for $N_2$ and C were defined as equivalent. Fits with more parameters yielded similar values in R-factor, but much larger $\chi_v^2$. This model structure is most consistent with an average coordination environment consisting of approximately two chelating ligands per uranyl and one $\mu^2$ bridging Ni, however, the large error for Ni coordination number and $\sigma^2$ suggests this model is not able to completely describe the data. It is likely fractional contributions from phosphate, carbonate, and different metal species, are necessary to improve the fit. Data were not fit beyond 3.5 Å in R-space due to the noise in the data.

**Table S12** Paths, Initial Path Lengths, Degeneracies, and Parameters for Fitting Polymer Fibres Contacted with Filtered Environmental Seawater for 56 Days

| **Scattering Path** | **$N_{degen}$** | **R(Å)** | **ΔR (Å)** | **$\sigma^2$ (Å$^2$)** | **$\Delta E_1$** |
|---|---|---|---|---|---|
| $U \rightarrow O_{yl}$ | 2 | 1.79 | $\Delta R\text{-}O_{yl}$ | $\sigma^2\text{-}O_{yl}$ | $\Delta E_1$ |
| $U \rightarrow O_1$ | CN_1 | 2.43 | ΔR-O | $\sigma^2$-O | $\Delta E_2$ |
| $U \rightarrow N_1$ | CN_1 | 2.56 | ΔR-O | $\sigma^2$-O | $\Delta E_2$ |
| $U \rightarrow N_2$ | CN_2 | 3.35 | ΔR-N | $\sigma^2$-N | $\Delta E_2$ |
| U→C | CN_2 | 3.48 | ΔR-N | $\sigma^2$-N | $\Delta E_2$ |
| U→Ni | CN_3 | 3.53 | ΔR-Ni | $\sigma^2$-Ni | $\Delta E_2$ |
| $U \rightarrow O_1 \rightarrow N_2$ | CN_2 | 3.56 | $0.5 \times \Delta R\text{-}O_1 + 0.5 \times \Delta R\text{-}N_2$ | $0.5 \times \sigma^2\text{-O} + 0.5 \times \sigma^2\text{-N}$ | $\Delta E_2$ |
| $U \rightarrow O_{yl(1)} \rightarrow O_{yl(2)}$ | 2 | 3.57 | $2 \times \Delta R\text{-}O_{yl}$ | $2 \times \sigma^2\text{-}O_{yl}$ | $\Delta E_1$ |
| $U \rightarrow O_{yl(1)} \rightarrow U \rightarrow O_{yl(2)}$ | 2 | 3.57 | $2 \times \Delta R\text{-}O_{yl}$ | $2 \times \sigma^2\text{-}O_{yl}$ | $\Delta E_1$ |
| $U \rightarrow O_{yl(1)} \rightarrow U \rightarrow O_{yl(1)}$ | 2 | 3.57 | $2 \times \Delta R\text{-}O_{yl}$ | $2 \times \sigma^2\text{-}O_{yl}$ | $\Delta E_1$ |
| $U \rightarrow O_{yl} \rightarrow N_1$ | 2×CN_1 | 3.60 | $0.5 \times \Delta R\text{-}O_{yl} + 0.5 \times \Delta R\text{-}N_1$ | $0.5 \times \sigma^2\text{-}O_{yl} + 0.5\times \sigma^2\text{-O}$ | $\Delta E_1$ |
| $U \rightarrow O_{yl} \rightarrow O_1$ | 2×CN_1 | 3.65 | $0.5 \times \Delta R\text{-}O_{yl} + 0.5 \times \Delta R\text{-}O_1$ | $0.5 \times \sigma^2\text{-}O_{yl} + 0.5\times \sigma^2\text{-O}$ | $\Delta E_1$ |
| $U \rightarrow N_1 \rightarrow C$ | 2×CN_2 | 3.70 | $0.5 \times \Delta R\text{-}N_1 + 0.5 \times \Delta R\text{-C}$ | $0.5 \times \sigma^2\text{-O} + 0.5\times \sigma^2\text{-N}$ | $\Delta E_2$ |

**Table** S13 Best Fit Values for Polymer Fibres Contacted with Filtered Environmental Seawater

| Scattering Path | $N_{degen}$ | R(Å) | error | | $\sigma^2$ (Å$^2$) | error |
|---|---|---|---|---|---|---|
| $U \rightarrow O_{yl}$ | 2[a] | 1.80 | 0.01 | | 0.002 | < 0.001 |
| $U \rightarrow O_1$ | 2.8 ± 0.6 | 2.40 | 0.02 | | 0.003 | 0.002 |
| $U \rightarrow N_1$ | 2.8 ± 0.6 | 2.56 | 0.02 | | 0.003 | 0.002 |
| $U \rightarrow N_2$ | 2.8 ± 0.2[b] | 3.41 | 0.07 | | 0.003 | 0.002 |
| $U \rightarrow C$ | 2.8 ± 0.2[b] | 3.54 | 0.07 | | 0.003 | 0.002 |
| $U \rightarrow Ni$ | 1 ± 1 | 3.41 | 0.04 | | 0.006 | 0.004 |
| $U \rightarrow O_1 \rightarrow N_2$ | 2.8 ± 0.3 | 3.59 | 0.04 | | 0.004 | 0.002 |
| $U \rightarrow O_{yl(1)} \rightarrow O_{yl(2)}$ | 2[a] | 3.61 | 0.01 | | 0.004 | 0.001 |
| $U \rightarrow O_{yl(1)} \rightarrow U \rightarrow O_{yl(2)}$ | 2[a] | 3.61 | 0.01 | | 0.004 | 0.001 |
| $U \rightarrow O_{yl(1)} \rightarrow U \rightarrow O_{yl(1)}$ | 2[a] | 3.61 | 0.01 | | 0.004 | 0.001 |
| $U \rightarrow O_{yl} \rightarrow N_1$ | 5.6 ± 0.3 | 3.70 | 0.01 | | 0.004 | 0.001 |
| $U \rightarrow O_{yl} \rightarrow O_1$ | 5.6 ± 0.3 | 3.70 | 0.01 | | 0.003 | 0.001 |
| $U \rightarrow N_1 \rightarrow C$ | 5.6± 0.3 | 3.72 | 0.04 | | 0.003 | 0.002 |
| $\Delta E_1 = 0 \pm 1$ eV | | | | | | |
| $\Delta E_2 = 2 \pm 2$ eV | | | | | | |

[a] The coordination number for $U \rightarrow O_{yl}$ was held at 2 for the model.

[b] The uncertainty in step height during normalization can be as large as 10%. As $S_0^2$, $N$, and step height are all components of the amplitude, the coordination number cannot be determined to greater accuracy than 10%.[18]

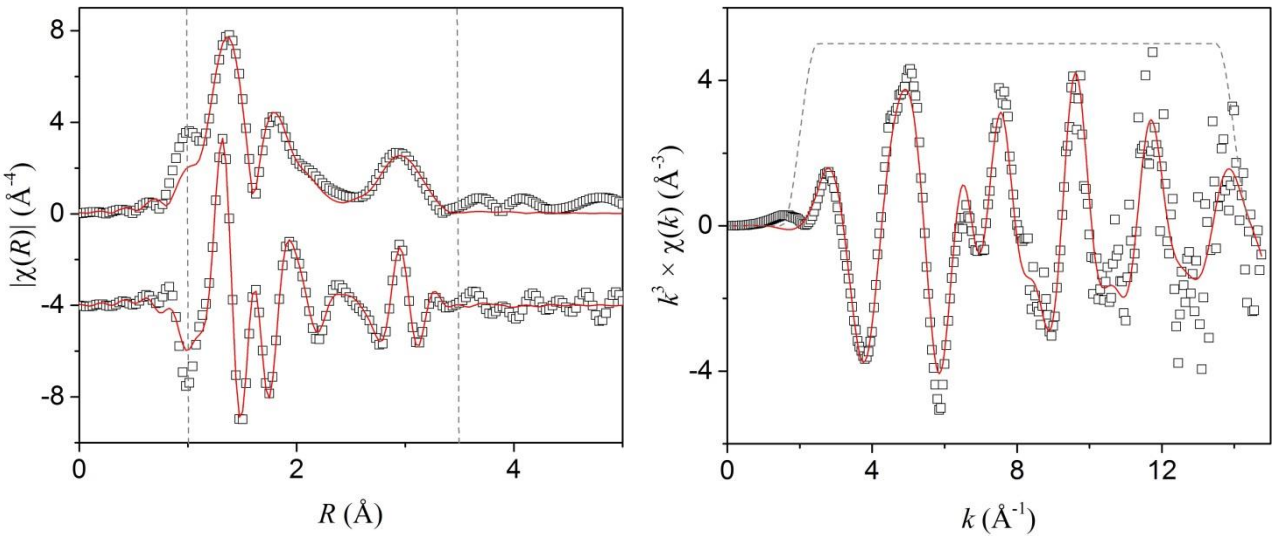


**Figure S13** Data (open symbols) and best-fit chelation model (line) for fit of EXAFS data for polymer fibres contacted with filtered environmental seawater for 56 days. The Fourier transform is displayed on the left, with the magnitude (top) and real components. The right column is plotted in k-space. All plots are displayed with $k^3$-weighting. Grey lines display the fitting window.

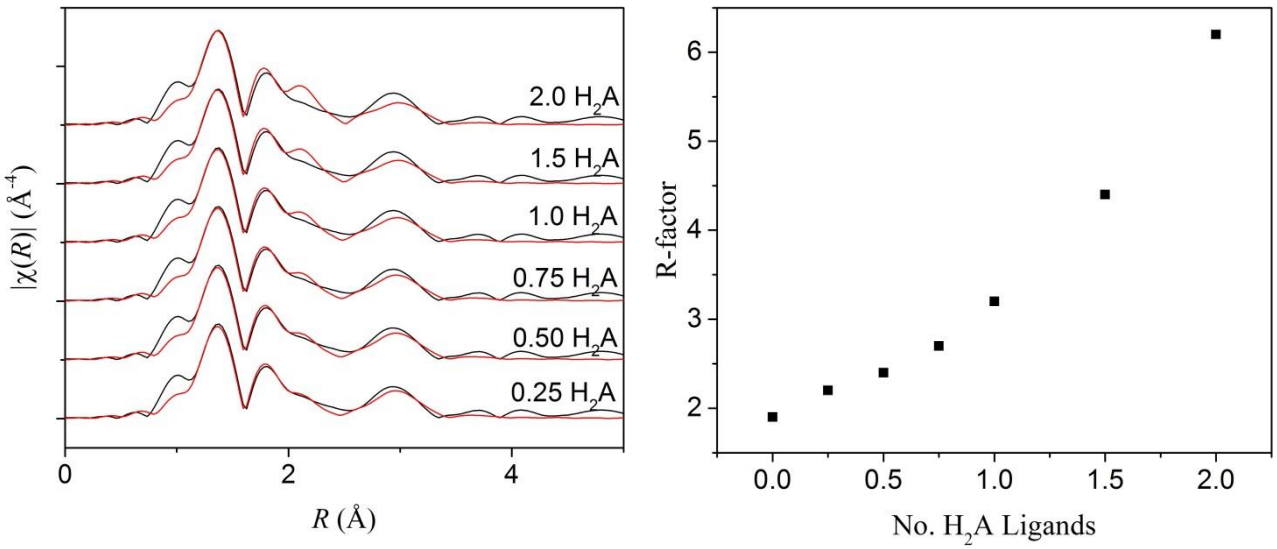


**Figure S14** Influence of cyclic imide dioxime (abbreviated in this figure as $H_2A$[7]) on fit of EXAFS data for seawater-contacted polymer fibers. (Left) Including the imide nitrogen of the tridentate-binding model results in a visibly worse fit with increasing contribution. (Right) R-factor as a function of number

of cyclic imide dioxime ligands included in the average fit. These R-factors correspond to the plots displayed in the left panel.

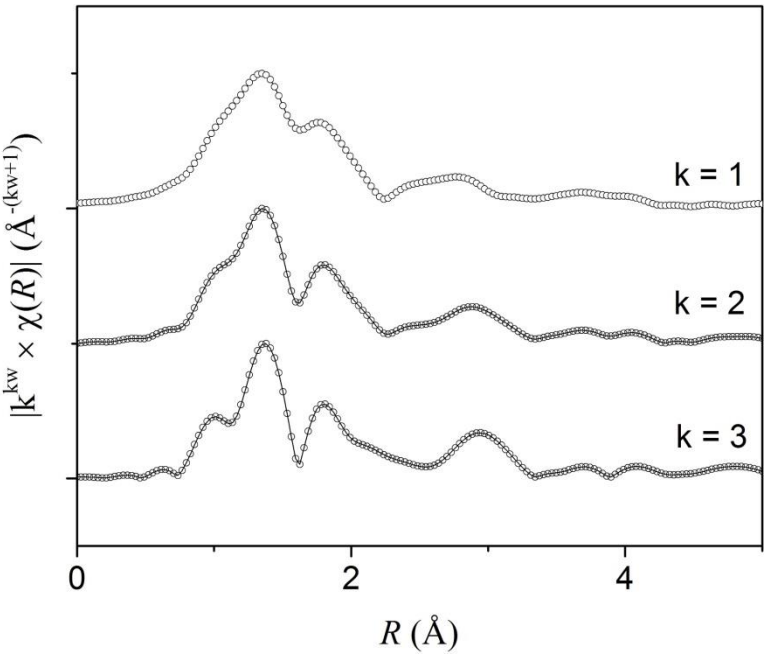


**Figure S15** EXAFS spectra for seawater-contacted polymer fibers displayed with k-weights of 1, 2, and 3. The increasing contribution of the feature at 3 Å at higher k-weighting is consistent with scattering from a higher Z-number element. All spectra were collected at room temperature.

*5.2.4 Seawater-Contacted Fibres (Post-Elution).* The data collected for seawater contacted fibres post-elution is significantly more noisy than any of the previously discussed samples. As a result, a smaller amount of data were used to perform the fit, restricting the number of parameters which could be used and directly impacting the fit metrics. The model used to fit the fibre data was constructed in a similar fashion to the simulant-contacted fibres. The first shell was composed exclusively of the tightly-bound uranyl axial oxygen ($O_{yl}$) with degeneracy fixed at 2. The second shell was composed of light scatterers at two different distances with equal, but variable degeneracy ($O_1$, $N_1$). The third shell was composed of light scatterers with variable degeneracy ($N_2$, C). $\Delta R$ and $\sigma^2$ were free parameters for all

direct scattering paths. Degeneracy was a free parameter for all direct scattering paths except $O_{yl}$. To comply with the Nyquist criterion, the degeneracy and $\sigma^2$ for $O_1$ and $N_1$ were defined as equivalent, and the degeneracy, $\Delta R$, and $\sigma^2$ for $N_2$ and C were defined as equivalent. Data were not fit beyond 3.5 Å in R-space due to the noise in the data.

**Table S14** Paths, Initial Path Lengths, Initial Degeneracies, and Parameters for Fitting Polymer Fibres Contacted Environmental Seawater and Eluted with Dilute HCl

| **Scattering Path** | **$N_{degen}$** | **R(Å)** | **$\Delta R$ (Å)** | **$\sigma^2$ (Å$^2$)** | **$\Delta E_1$** |
|---|---|---|---|---|---|
| $U \rightarrow O_{yl}$ | 2 | 1.79 | $\Delta R\text{-}O_{yl}$ | $\sigma^2\text{-}O_{yl}$ | $\Delta E_1$ |
| $U \rightarrow O_1$ | CN_1 | 2.43 | $\Delta R\text{-}O$ | $\sigma^2\text{-}O$ | $\Delta E_2$ |
| $U \rightarrow N_1$ | CN_1 | 2.53 | $\Delta R\text{-}O$ | $\sigma^2\text{-}O$ | $\Delta E_2$ |
| $U \rightarrow N_2$ | CN_2 | 3.36 | $\Delta R\text{-}N$ | $\sigma^2\text{-}N$ | $\Delta E_2$ |
| $U \rightarrow C$ | CN_2 | 3.47 | $\Delta R\text{-}C$ | $\sigma^2\text{-}C$ | $\Delta E_2$ |
| $U \rightarrow O_1 \rightarrow N_2$ | CN_2 | 3.57 | $0.5 \times \Delta R\text{-}O_1 + 0.5 \times \Delta R\text{-}N_2$ | $0.5 \times \sigma^2\text{-}O + 0.5 \times \sigma^2\text{-}N$ | $\Delta E_2$ |
| $U \rightarrow O_{yl(1)} \rightarrow O_{yl(2)}$ | 2 | 3.57 | $2 \times \Delta R\text{-}O_{yl}$ | $2 \times \sigma^2\text{-}O_{yl}$ | $\Delta E_1$ |
| $U \rightarrow O_{yl(1)} \rightarrow U \rightarrow O_{yl(2)}$ | 2 | 3.57 | $2 \times \Delta R\text{-}O_{yl}$ | $2 \times \sigma^2\text{-}O_{yl}$ | $\Delta E_1$ |
| $U \rightarrow O_{yl(1)} \rightarrow U \rightarrow O_{yl(1)}$ | 2 | 3.57 | $2 \times \Delta R\text{-}O_{yl}$ | $2 \times \sigma^2\text{-}O_{yl}$ | $\Delta E_1$ |
| $U \rightarrow O_1 \rightarrow N_1$ | 2×CN_1 | 3.67 | $0.5 \times \Delta R\text{-}O_1 + 0.5 \times \Delta R\text{-}N_1$ | $0.5 \times \sigma^2\text{-}O_{yl} + 0.5\times \sigma^2\text{-}O$ | $\Delta E_2$ |

**Table S15** Best Fit Values for Polymer Fibres Contacted with Filtered Environmental Seawater and Eluted with Dilute HCl

| Scattering Path | $N_{degen}$ | R(Å) | error | | $\sigma^2$ (Å$^2$) | error |
|---|---|---|---|---|---|---|
| $U \rightarrow O_{yl}$ | 2[a] | 1.80 | 0.01 | | 0.002 | < 0.001 |
| $U \rightarrow O_1$ | 3.0 ± 1.2 | 2.38 | 0.02 | | 0.006 | 0.006 |
| $U \rightarrow N_1$ | 3.0 ± 1.2 | 2.51 | 0.02 | | 0.006 | 0.006 |
| $U \rightarrow N_2$ | 3.0 ± 0.3 | 3.38 | 0.04 | | 0.006 | 0.004 |
| $U \rightarrow C$ | 3.0 ± 0.3 | 3.49 | 0.02 | | 0.006 | 0.004 |
| $U \rightarrow O_1 \rightarrow N_2$ | 3.0 ± 0.3 | 3.56 | 0.02 | | 0.006 | 0.004 |
| $U \rightarrow O_{yl(1)} \rightarrow O_{yl(2)}$ | 2[a] | 3.61 | 0.01 | | 0.004 | 0.001 |
| $U \rightarrow O_{yl(1)} \rightarrow U \rightarrow O_{yl(2)}$ | 2[a] | 3.61 | 0.01 | | 0.004 | 0.001 |
| $U \rightarrow O_{yl(1)} \rightarrow U \rightarrow O_{yl(1)}$ | 2[a] | 3.61 | 0.01 | | 0.004 | 0.001 |
| $U \rightarrow O_1 \rightarrow N_1$ | 6.0 ± 2.4 | 3.65 | 0.01 | | 0.006 | 0.006 |
| $\Delta E_1 = 4 \pm 2$ eV | | | | | | |
| $\Delta E_2 = 0 \pm 4$ eV | | | | | | |

[a] The coordination number for $U \rightarrow O_{yl}$ was held at 2 for the model.

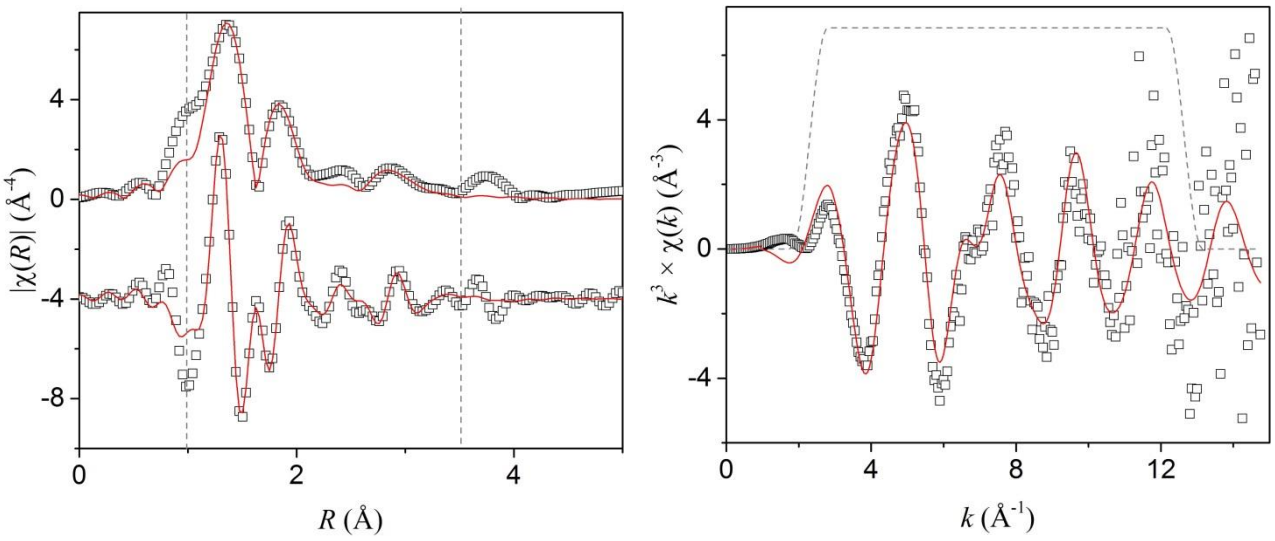


**Figure S16** Data (open symbols) and best-fit chelation model (line) for fit of EXAFS data for polymer fibres contacted with filtered environmental seawater for 56 days, then eluted with dilute HCl. The Fourier transform is displayed on the left, with the magnitude (top) and real components. The right

column is plotted in k-space. All plots are displayed with $k^3$-weighting. Grey lines display the fitting window.

## 6 X-ray Photoelectron Spectroscopy

Polyethylene pellets were hot-pressed to generate a polyethylene film. The film was then grafted by irradiation graft polymerization (RIGP) as previously reported for the fibrous adsorbent. (REF 39 of manuscript) The polyethylene fllm was then contacted with a brine containing 6-8 ppm uranium as uranyl nitrate hexahydrate (17 mg, 0.034 mmol) with sodium chloride (25.6 g, 0.44 mol) and sodium bicarbonate (194 mg, 2.3 mmol) in 1 L of deionized water. This affords a uranyl brine that contains the seawater relevant concentrations of sodium chloride and bicarbonate while increasing the amount of uranium to enhance the sorption kinetics. X-ray photoelectron spectroscopy (XPS) data were collecte using a PHI 3056 spectrometer with an Al anode source operated at 15 kV and an applied power of 350 W. Adventitious carbon was used to calibrate the binding energy shifts of the sample C1s = 284.8 eV. High resolution data was collected at pass energy of 5.85 eV with 0.05 eV step sizes and a minimum of 60 scans to improve the signal to noise ratio; lower resolution survey scans were collected at pass energy of 93.5 eV with 0.5 eV step sizes and a minimum of 25 scans.

The collected XPS data from the grafted polyethylene film is shown in Figure S13. The surface consisted of 5 at% N, 2.5 at% Na, 0.6 at% U, 8.9 at% O, 27.0% F, with the balance carbon. The primary U $4f_{7/2}$ species has a binding energy of 381.6 eV which is attributed to an $U^{6+}$ species adsorbed from solution.[21] There is a second higher energy U 4f species located at 384.2 eV likely due to $U^{6+}$-OH or $U^{6+}$-O-Na. The N1s data shows the presence of two N species. The first species with a binding energy of 398.7 eV is due to a $H_2N$-C=*N*-OH iminic nitrogen. The second species, 399.7 eV, is due to the $H_2$*N*-C=N-OH nitrogen.[22, 23]

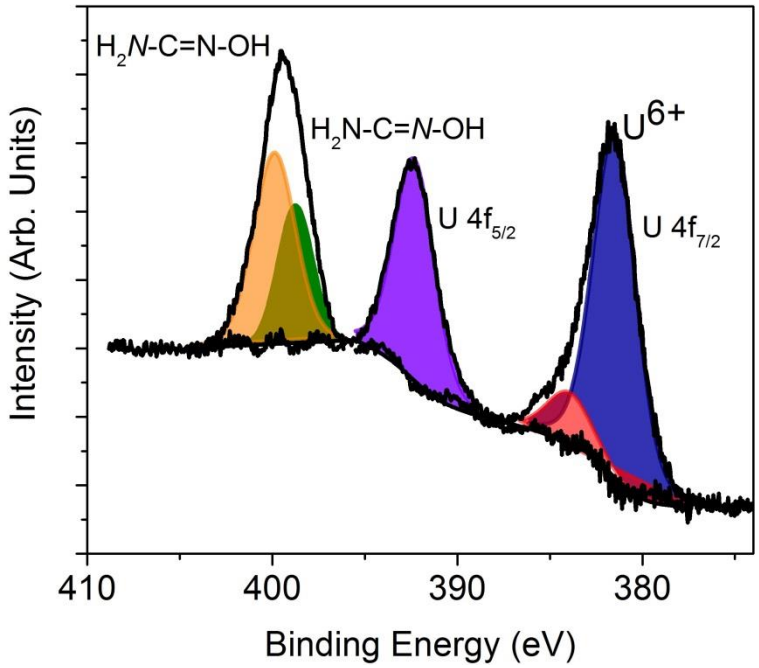


**Figure S17** XPS spectra and fit for poly-acetamidoxime film saturated with uranyl in DI water.

### 7. Differential Pair Distribution Function

Pair distribution spectra (PDF) were obtained on samples cryogenically pulverized as discussed in section 3.1. Powdered samples were packed in a Kapton tube approximately 15 mm in length and 0.0320" ID. Each end of the tube was sealed with epoxy. This sealed tube was then placed in a second Kapton tube, approximately 20 mm in length and 0.0395" ID. Again, each end was sealed with epoxy. This manner of secondary containment was sufficient for measurement of radiological samples at the Advanced Photon Source. Data were collected at 58.88 keV on beamline 11ID-B. The detector was positioned 19.556 cm from the sample as determined by calibration against a $CeO_2$ standard. Three data sets were obtained for each sample, consisting of 100 frames each, collected over 3 seconds per frame. Raw images were processed using Fit-2D[24] and PDFs were extracted as discussed elsewhere.[25]

Differential pair distribution function (d-PDF) analysis was performed, where the difference between two PDF spectra is obtained through direct subtraction of the reference PDF spectrum (Figure S18).[26] Using the pristine adsorbent as a reference PDF spectrum, d-PDF spectra were obtained for both

seawater-contacted fibres and HCl-eluted fibres. The d-PDF spectrum was also obtained between the seawater-contacted fibres and the HCl-eluted fibres.

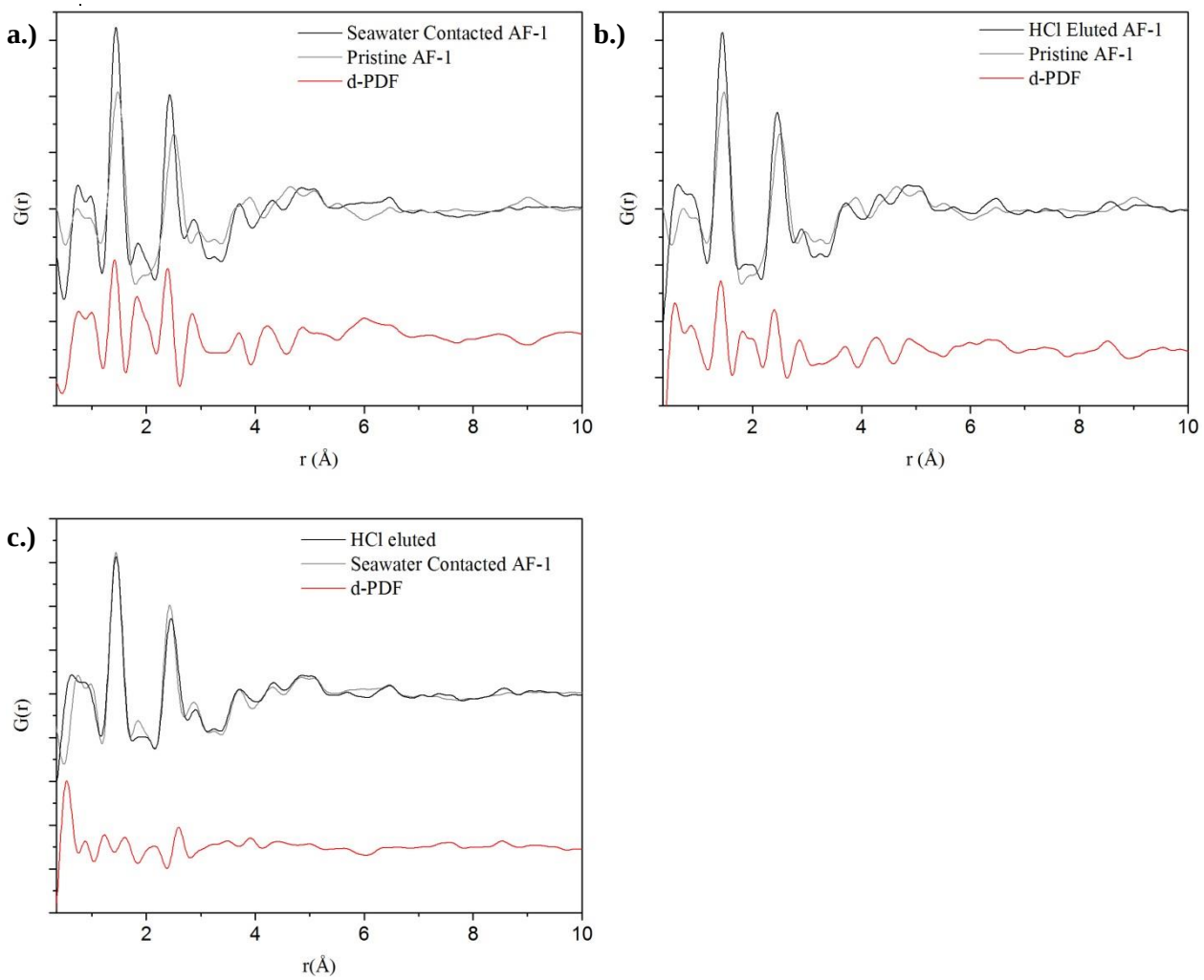


**Figure S18** PDF and d-PDF spectra for amidoxime-functionalized fibres. Plot a) displays the d-PDF between seawater-contacted fibers and pristine fibres, while b) displays the d-PDF for HCl-eluted fibres and pristine fibres. Plot c) presents the d-PDF between HCl-eluted fibres and seawater-contacted fibres. In all instances, the reference spectra is plotted in grey and is subtracted from the spectra plotted in black to obtain the d-PDF spectra, plotted in red.

Analysis of d-PDF spectra for both seawater-contacted fibres and HCl-eluted fibres reveal the most significant probability differences occur at bond lengths of 1.5, 1.8, 2.5, and 3 Å. It is encouraging that the distance between U-$O_{yl}$ is approximately 1.8 Å, the distance between U and the first shell scatterers is approximately 2.5 Å, and a feature is apparent at approximately 3.5 Å where XAFS fits suggest the presence of a $\mu^2$-oxo bridged transition metal. Moreover, these features are largely absent in

the d-PDF between seawater-contacted and HCl-eluted fibres, consistent with an amidoxime-bound uranium and an eluted transition metal. Nevertheless, definitive identification of structural features is not possible, due to the large number of metals bound by the seawater contacted fibres (see Table S2). The increased bond length probability can also be attributed to interactions with transition metals that are not eluted with HCl (specifically V and Cu), as well as the alkali and alkali earth cations (Na, Mg, Ca) which are ubiquitous in seawater.[2, 4]

## 8. Computational

### *8.1. Methods*

Density functional theory (DFT) calculations were carried out using the Gaussian 09 Revision D.01.[27] Moller-Plesset perturbation theory (MP2)[28, 29] and coupled-cluster theory calculations with singles, doubles, and perturbative triples excitations (CCSD(T))[30-32] were performed with the NWChem 6.5 software package.[33] The standard Stuttgart small-core (SSC) 1997 relativistic effective core potential (RECP) was used for uranium, replacing 60 core electrons to account for scalar relativistic effects.[34] The valence electrons in this basis set are represented by a contracted [8s/7p/6d/4f] basis. The most diffuse function on uranium (exponent 0.005) was removed to improve SCF convergence. The basis set for the light atoms was 6-311++G(d,p) and aug-cc-pVDZ in DFT and post-Hartree-Fock methods, respectively. Geometry optimizations were performed at the MP2 and B3LYP levels. [28, 29, 35, 36] Single-point CCSD(T)/SSC/aug-cc-pVDZ calculations using B3LYP/SSC/6-311++G(d,p) and MP2/SSC/aug-cc-pVDZ geometries were employed to determine the benchmark relative energies of $UO_2^{2+}$ complexes with formamidoxime in the $\eta^2$ and chelate binding motifs and to determine the sensitivity of the CCSD(T) relative energies to changes in geometries of uranyl complexes at different level of theories. Only the valence electrons were correlated in the MP2 and CCSD(T) calculations. Frequency calculations were performed at the B3LYP/SSC/6-31+G(d) level to verify that geometries were minima and to compute zero point energies and thermal corrections using the rigid rotor-harmonic oscillator approximation, except that vibrational frequencies lower than 60 $cm^{-1}$ were raised to 60 $cm^{-1}$. This procedure is similar to that proposed by Truhlar and co-workers[37] to correct for the well-known breakdown of the harmonic

oscillator model for the free energies of low-frequency vibrational modes. Using the gas phase geometries, implicit solvent corrections were obtained at the B3LYP/SSC/6-31+G(d) level using the IEF-PCM[38-40] solvation model in Gaussian.[27] Since only the first coordination shell was treated explicitly in this study, it was possible to perform a systematic search of low-energy clusters for a given composition. The results are reported using the lowest energy clusters identified at the B3LYP/SSC/6-311++G(d,p) level for a given stoichiometry and binding motif.

*8.2. Analysis of the computational results*

In this work, we employ high level coupled-cluster CCSD(T)/aug-cc-pVDZ calculations to investigate the potential binding motifs of uranyl complexes with formamidoxime ligands. The chosen ligand is small enough that high-level *ab initio* calculations can be readily performed. Relative energies obtained from CCSD(T) calculations are used as benchmarks against DFT and MP2 predicted energies. The most stable five- and six-coordinate B3LYP geometries of the uranyl complexes with 1−3 ligands involving $\eta^2$-binding with the N-O bond and chelation through the oxime oxygen and amine nitrogen donor atoms are shown in Figure S14. Consistent with previous DFT calculations and X-ray diffraction data,[1, 5, 41] the $\eta^2$ binding motif is the most stable at the B3LYP and MP2 levels for all amidoxime complexes. The results given in Table S16 indicate that the presence of one chelate motif destabilized the complex by 2.8−5.1 kcal/mol at the B3LYP and by 1.9−4.7 kcal/mol at the MP2 level. However, after the application of the CCSD(T) correction, the difference in energy between the two binding forms becomes much smaller. In particular, a five-coordinate 1:2 uranyl complex with a mixed coordination of the two ligands, $[UO_2(ao\text{-}\eta^2)(ao\text{-chelate})(H_2O)]$ is slightly more stable than that with pure $\eta^2$ coordination, $[UO_2(ao\text{-}\eta^2)_2(H_2O)]$ at the CCSD(T) level. The high consistency of the CCSD(T) results obtained with B3LYP and MP2 geometries (within 0.4 kcal/mol of each other) indicates that the CCSD(T) relative energies are not particularly sensitive to the choice of the geometry obtained at different levels of theory. In summary, analysis of the relative stabilities of uranyl complexes with amidoxime with the effect of higher order correlation estimated at the coupled-cluster theory reveals that the difference in the stability

of the $\eta^2$ and chelate binding motifs is smaller than previously thought based on DFT calculations[5] and both forms may coexist in thermodynamic equilibrium in aqueous solution.

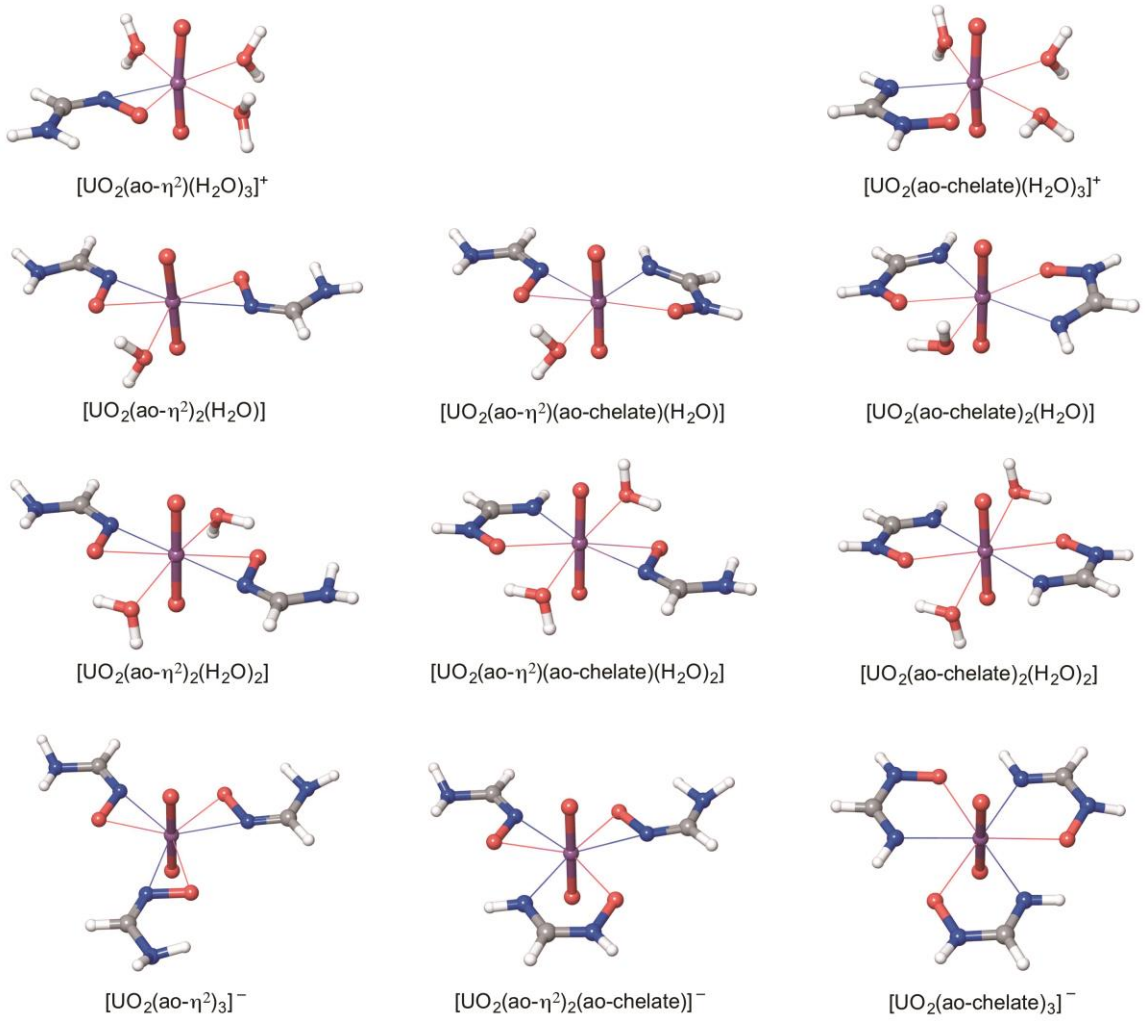


**Figure S19.** Structures of uranyl complexes with formamidoxime (ao), $[UO_2(ao)_x(H_2O)_y]^{2-x}$, obtained after geometry optimization at the B3LYP/SSC/6-311++G(d,p) level of theory.

**Table S16.** Relative stabilities of $[UO_2(ao)_x(H_2O)_y]^{2-x}$ complexes obtained in the solvent reaction field at several levels of theory ($\Delta G_{aq}$ in kcal/mol).[a] Structures of the representative complexes are shown in Figure S16.

| stoichiometry/binding mode | B3LYP[b] | MP2[c] | CCSD(T)// B3LYP[d] | CCSD(T)// MP2[d] |
|---|---|---|---|---|
| $[UO_2(ao\text{-}\eta^2)(H_2O)_3]^+$ | 0.00 | 0.00 | 0.00 | 0.00 |

| | | | | |
|---|---|---|---|---|
| $[UO_2(ao\text{-}chelate)(H_2O)_3]^+$ | 5.10 | 3.27 | 1.23 | 0.96 |
| | | | | |
| $[UO_2(ao\text{-}\eta^2)_2(H_2O)]$ | 0.00 | 0.00 | 0.34 | 0.03 |
| $[UO_2(ao\text{-}\eta^2)(ao\text{-}chelate)(H_2O)]$ | 3.07 | 1.93 | 0.00 | 0.00 |
| $[UO_2(ao\text{-}chelate)_2(H_2O)]$ | 9.03 | 7.21 | 3.48 | 3.16 |
| | | | | |
| $[UO_2(ao\text{-}\eta^2)_2(H_2O)_2]$ | 0.00 | 0.00 | 0.00 | 0.00 |
| $[UO_2(ao\text{-}\eta^2)(ao\text{-}chelate)(H_2O)_2]$ | 4.96 | 4.67 | 2.85 | 2.92 |
| $[UO_2(ao\text{-}chelate)_2(H_2O)_2]$ | 13.5 | 13.9 | 10.1 | 10.3 |
| | | | | |
| $[UO_2(ao\text{-}\eta^2)_3]^-$ | 0.00 | 0.00 | 0.00 | 0.0 |
| $[UO_2(ao\text{-}\eta^2)_2(ao\text{-}chelate)]^-$ | 2.84 | 2.17 | 1.28 | 1.32 |
| $[UO_2(ao\text{-}\eta^2)(ao\text{-}chelate)_2]^-$ | 9.31 | 8.15 | 6.19 | 6.34 |
| $[UO_2(ao\text{-}chelate)_3]^-$ | 21.3 | 21.6 | 17.8 | 18.2 |

[a]Zero point energies, thermal corrections, and solvent corrections using the IEF-PCM solvation model were calculated at the B3LYP/SSC/6-31+G(d) level. [b]B3LYP/SSC/6-311++G(d,p). [c]MP2/SSC/aug-cc-pVDZ. [d]Single-point CCSD(T)/SSC/aug-cc-pVDZ energies on either B3LYP/SSC/6-311++G(d,p) or MP2/SSC/aug-cc-pVDZ optimized geometries.

**9. Crystallography**

Single crystal X-ray diffraction of uranyl benzamidoxime was performed with a Bruker D8 Venture, dual microsource (Cu and Mo) diffractometer with a CMOS detector. Mo Kα radiation was used. The frames were integrated with the Bruker SAINT© build in the APEX II software package using a narrow-frame integration algorithm, which also corrects for the Lorentz and polarization effects. Absorption corrections were applied using SADABS. Structures were solved by direct methods and refined to convergence by the least squares method on $F^2$ using the SHELXTL-2013 software suite.[42] All non-hydrogen atoms were refined anisotropically except for the solvent molecule. The crystal structure is available from the Cambridge Crystallographic Database, number 1419942.

**Table S17.** Crystallographic information.

| | |
|---|---|
| Name | Uranyl Benzamidoxime |
| Formula | UC16H22N4O6 |
| Fw | 604.41 |
| Temperature (K) | 100.0 |
| Wavelength (Å) | 0.71073 |
| Crystal system | monoclinic |
| Space group | $P2_1/c$ |
| *a*, Å | 10.4376(8) |
| *b*, Å | 5.7148(4) |
| *c*, Å | 15.9916(11) |
| α, ° | 90 |
| β, ° | 102.543(2) |
| γ, ° | 90 |
| *V*, Å$^3$ | 931.11(12) |
| *Z* | 2 |
| Density (calcd. g/cm$^3$) | 2.156 |
| Absorption coeff. (mm$^{-1}$) | 8.758 |
| F(000) | 572 |
| θ range data collection | 2.610 – 27.155 |
| Limiting indices | $-13 \leq h \leq 13$ |
| | $-7 \leq k \leq 7$ |
| | $-20 \leq l \leq 20$ |
| Reflection collected | 11878 |
| Independent reflections | 2068 |
| R(int) | 0.0685 |
| Data/restraints/parameters | 2068/1/129 |
| Goodness-of-fit on $F^2$ | 1.043 |
| Final R indices [I>2σ(I)] | R1 = 0.0288, wR2 = 0.0485 |
| R indices (all data) | R1 = 0.0613, wR2 = 0.0550 |

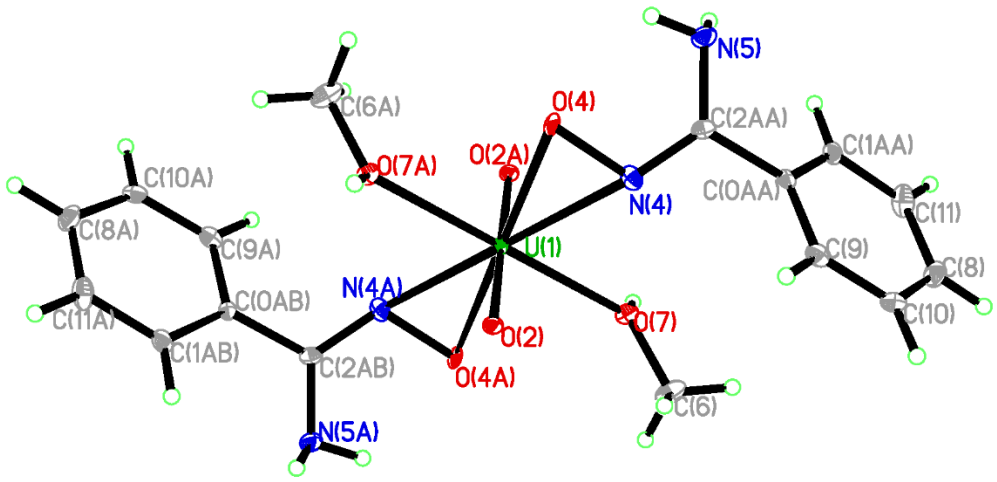


**Figure S20.** ORTEP of Uranyl Benzamidoxime at 50% probability.

## 10. References


1. S. P. Kelley, P. S. Barber, P. H. K. Mullins and R. D. Rogers, *Chem. Commun.*, 2014, **50**, 12504-12507.
2. J. Kim, C. Tsouris, R. T. Mayes, Y. Oyola, T. Saito, C. J. Janke, S. Dai, E. Schneider and D. Sachde, *Sep. Sci. Technol.*, 2013, **48**, 367-387.
3. J. Kim, Y. Oyola, C. Tsouris, C. R. Hexel, R. T. Mayes, C. J. Janke and S. Dai, *Ind. Eng. Chem. Res.*, 2013, **52**, 9433-9440.
4. J. Kim, C. Tsouris, Y. Oyola, C. J. Janke, R. T. Mayes, S. Dai, G. Gill, L.-J. Kuo, J. Wood, K.-Y. Choe, E. Schneider and H. Lindner, *Ind. Eng. Chem. Res.*, 2014, **53**, 6076-6083.
5. S. Vukovic, L. A. Watson, S. O. Kang, R. Custelcean and B. P. Hay, *Inorg. Chem.*, 2012, **51**, 3855-3859.
6. *US Pat.*, 2009.
7. G. Tian, S. Teat, Z. Zhang and L. Rao, *Dalton. Trans.*, 2012, **41**, 11579-11586.
8. S. O. Kang, S. Vukovic, R. Custelcean and B. P. Hay, *Ind. Eng. Chem. Res.*, 2012, **51**, 6619-6624.
9. A. Zhang, T. Asakura and G. Uchiyama, *React. Funct. Polym.*, 2003, **57**, 67-76.
10. S. Katragadda, H. D. Gesser and A. Chow, *Talanta*, 1997, **45**, 257-263.
11. A. Zhang, G. Uchiyama and T. Asakura, *Sep. Sci. Technol.*, 2003, **38**, 1829-1849.
12. N. Seko, A. Katakai, M. Tamada, T. Sugo and F. Yoshii, *Sep. Sci. Technol.*, 2004, **39**, 3753-3767.
13. T. Suzuki, K. Saito, T. Sugo, H. Ogura and K. Oguma, *Anal. Sci.*, 2000, **16**, 429-432.
14. B. L. Henke, E. M. Gullikson and J. C. Davis, *At. Data Nucl. Data Tables*, 1993, **54**, 181-342.
15. B. Ravel and M. Newville, *J. Synchrotron Radiat.*, 2005, **12**, 537-541.
16. J. J. Rehr and R. C. Albers, *Rev. Mod. Phys.*, 2000, **72**, 621-654.
17. S. D. Kelly, D. Hesterberg and B. Ravel, in *Methods of Soil Analysis*, eds. A. L. Ulery and L. R. Drees, Soil Science Society of America, Madison, WI, 2008, vol. 5, ch. 14, pp. 387 - 463.
18. S. D. Kelly, K. M. Kemner, J. B. Fein, D. A. Fowle, M. I. Boyanov, B. A. Bunker and N. Yee, *Geochim. Cosmochim. Acta*, 2002, **66**, 3855-3871.
19. S. Calvin, *XAFS for Everyone*, CRC Press, Boca Raton, FL, 2013.

20. C. Den Auwer, E. Simoni, S. Conradson and C. Madic, *Eur. J. Inorg. Chem.*, 2003, **2003**, 3843-3859.
21. E. S. Ilton and P. S. Bagus, *Surf. Interface Anal.*, 2011, **43**, 1549-1560.
22. J. Gorka, R. T. Mayes, L. Baggetto, G. M. Veith and S. Dai, *J. Mater. Chem. A*, 2013, **1**, 3016-3026.
23. H.-w. Yu, S.-s. Yang, H.-m. Ruan, J.-n. Shen, C.-j. Gao and B. Van der Bruggen, *Appl. Clay Sci.*, 2015, **111**, 67-75.
24. A. P. Hammersley, S. O. Svensson, M. Hanfland, A. N. Fitch and D. Hausermann, *High Pressure Research*, 1996, **14**, 235-248.
25. P. J. Chupas, X. Qiu, J. C. Hanson, P. L. Lee, C. P. Grey and S. J. L. Billinge, *J. Appl. Crystallogr.*, 2003, **36**, 1342-1347.
26. K. W. Chapman, P. J. Chupas and C. J. Kepert, *J. Am. Chem. Soc.*, 2005, **127**, 11232-11233.
27. M. J. Frisch, G. W. Trucks, H. B. Schlegel, G. E. Scuseria, M. A. Robb, J. R. Cheeseman, G. Scalmani, V. Barone, B. Mennucci, G. A. Petersson, H. Nakatsuji, M. Caricato, X. Li, H. P. Hratchian, A. F. Izmaylov, J. Bloino, G. Zheng, J. L. Sonnenberg, M. Hada, M. Ehara, K. Toyota, R. Fukuda, J. Hasegawa, M. Ishida, T. Nakajima, Y. Honda, O. Kitao, H. Nakai, T. Vreven, J. A. Montgomery, Jr. , J. E. Peralta, F. Ogliaro, M. Bearpark, J. J. Heyd, E. Brothers, K. N. Kudin, V. N. Staroverov, R. Kobayashi, J. Normand, K. Raghavachari, A. Rendell, J. C. Burant, S. S. Iyengar, J. Tomasi, M. Cossi, N. Rega, M. J. Millam, M. Klene, J. E. Knox, J. B. Cross, V. Bakken, C. Adamo, J. Jaramillo, R. Gomperts, R. E. Stratmann, O. Yazyev, A. J. Austin, R. Cammi, C. Pomelli, J. W. Ochterski, R. L. Martin, K. Morokuma, V. G. Zakrzewski, G. A. Voth, P. Salvador, J. J. Dannenberg, S. Dapprich, A. D. Daniels, Ö. Farkas, J. B. Foresman, J. V. Ortiz, J. Cioslowski and D. J. Fox, *Journal*, 2009.
28. C. Møller and M. S. Plesset, *Physical Review*, 1934, **46**, 618-622.
29. M. Head-Gordon, J. A. Pople and M. J. Frisch, *Chem. Phys. Lett.*, 1988, **153**, 503-506.
30. G. D. Purvis and R. J. Bartlett, *J. Chem. Phys.*, 1982, **76**, 1910-1918.
31. K. Raghavachari, G. W. Trucks, J. A. Pople and M. Head-Gordon, *Chem. Phys. Lett.*, 1989, **157**, 479-483.
32. J. D. Watts, J. Gauss and R. J. Bartlett, *J. Chem. Phys.*, 1993, **98**, 8718-8733.
33. M. Valiev, E. J. Bylaska, N. Govind, K. Kowalski, T. P. Straatsma, H. J. J. Van Dam, D. Wang, J. Nieplocha, E. Apra, T. L. Windus and W. A. de Jong, *Comput. Phys. Commun.*, 2010, **181**, 1477-1489.
34. M. Dolg, H. Stoll, H. Preuss and R. M. Pitzer, *J. Phys. Chem.*, 1993, **97**, 5852-5859.
35. A. D. Becke, *J. Chem. Phys.*, 1993, **98**, 5648-5652.
36. C. Lee, W. Yang and R. G. Parr, *Phys. Rev. [Sect.] B*, 1988, **37**, 785-789.
37. R. F. Ribeiro, A. V. Marenich, C. J. Cramer and D. G. Truhlar, *J. Phys. Chem. B*, 2011, **115**, 14556-14562.
38. S. Miertuš, E. Scrocco and J. Tomasi, *Chem. Phys.*, 1981, **55**, 117-129.
39. E. Cancès, B. Mennucci and J. Tomasi, *J. Chem. Phys.*, 1997, **107**, 3032-3041.
40. B. Mennucci, E. Cancès and J. Tomasi, *J. Phys. Chem. B*, 1997, **101**, 10506-10517.
41. P. S. Barber, S. P. Kelley and R. D. Rogers, *RSC. Adv.*, 2012, **2**, 8526-8530.
42. G. Sheldrick, *Acta Crystallogr. Sect. A: Found. Crystallogr.*, 2008, **64**, 112-122.